



저작자표시-동일조건변경허락 2.0 대한민국

이용자는 아래의 조건을 따르는 경우에 한하여 자유롭게

- 이 저작물을 복제, 배포, 전송, 전시, 공연 및 방송할 수 있습니다.
- 이차적 저작물을 작성할 수 있습니다.
- 이 저작물을 영리 목적으로 이용할 수 있습니다.

다음과 같은 조건을 따라야 합니다:



저작자표시. 귀하는 원저작자를 표시하여야 합니다.



동일조건변경허락. 귀하가 이 저작물을 개작, 변형 또는 가공했을 경우에는, 이 저작물과 동일한 이용허락조건하에서만 배포할 수 있습니다.

- 귀하는, 이 저작물의 재이용이나 배포의 경우, 이 저작물에 적용된 이용허락조건을 명확하게 나타내어야 합니다.
- 저작권자로부터 별도의 허가를 받으면 이러한 조건들은 적용되지 않습니다.

저작권법에 따른 이용자의 권리는 위의 내용에 의하여 영향을 받지 않습니다.

이것은 [이용허락규약\(Legal Code\)](#)을 이해하기 쉽게 요약한 것입니다.

[Disclaimer](#)

工學博士學位論文

스크린 프린팅에 의해 제작된 ZnS계
박막필름의 불순물 첨가에 의한
전계발광 효과에 관한 연구



2012년 2월

釜慶大學校大學院

印刷工學科

孫鳳均

On Electroluminescence effect of
impurity ZnS thin film structure
fabricated by Screen Printing Method
(스크린 프린팅에 의해 제작된
ZnS계 박막필름의 불순물 첨가에 의한
전계발광 효과에 관한 연구)

Advisor: Prof. Sang-Nam LEE

by

Pong-kyun SHON

A thesis submitted in partial fulfillment of the requirements
for the degree of Doctor of Philosophy

in Department of Graphic Arts Information Engineering,
The Graduate School, Pukyong National University

January 2012

손봉균의 工學博士 學位論文을 認准함.

2012年 2月 24日



主	審	理學博士	金 光 鐵	(印)
委	員	工學博士	南 壽 龍	(印)
委	員	工學博士	金 鐘 守	(印)
委	員	工學博士	申 東 崙	(印)
委	員	理學博士	李 相 南	(印)

CONTENTS

LIST OF FIGURES.....	ii
ABSTRACT.....	v
1. INTRODUCTION.....	1
2. THEORY.....	6
3. LITERATURE REVIEW.....	21
4. EXPERIMENTAL PROCEDURES	55
4.1. Material preparation for the EL film structure	55
4.1.1. ZnS-based phosphor added Carbon Nanotubes.....	55
4.1.2. ZnS-based phosphor inserted TCO.....	55
4.2. Fabrication of the EL film structure	56
5. RESULTS AND DISCUSSION.....	60
5.1. CNT doped ZnS based EL Devices	60
5.2. TCO doped ZnS based EL Devices.....	65
6. CONCLUSIONS.....	75
REFERENCES.....	77
국문요약.....	82

LIST OF FIGURES

Fig.1. Electroluminescence process for AC thin film EL device.....	6
Fig.2. Energy band diagram showing the mechanism of two electron tunneling.....	7
Fig.3. Mechanism showing the impact excitation and impact ionization.....	10
Fig.4. Energy diagram showing radiative and non-radiative de-excitation path.....	11
Fig.5. Energy band diagram showing Donor-Acceptor (DA) pair transition.....	13
Fig.6. Separation of an electron and hole pair under applied voltage.....	14
Fig.7. Schematic showing electron-hole recombination mechanisms.....	15
Fig.8. Crystal field splitting of d-orbital by octahedral and tetrahedral symmetry.....	19
Fig.9. Schematic showing released paste on mesh but not permeable into mesh.....	21
Fig.10. Schematic showing permeable part of paste by squeegee stroke.....	21
Fig.11. Schematic showing printed layer after finishing squeegee stroke.....	22
Fig.12. Schematic showing the paste separation from screen to substrate.....	22
Fig.13. Length side view showing the deformation of screen mesh.....	23
Fig.14. Width side view showing the deformation of screen mesh.....	24

Fig.15.		
Schematic illustrating patterning thickness for printed electronic industry.....		24
Fig.16.		
Schematic representation of ink jet printing process.....		29
Fig.17.		
Effect of droplet spacing on final printed line morphology.....		33
Fig.18.		
Schematic representation of gravure printing process.....		35
Fig.19.		
Photoluminescence characteristics of ZnS :(Cu, Al) pure phosphor.....		40
Fig.20.		
Energy band gap diagram of ZnS:(Cu, Al) phosphor.....		41
Fig.21.		
Electroluminescence mechanism of ZnS:(Cu, Al).....		42
Fig.22.		
Example of useful TCO compound material.....		46
Fig.23.		
Resistivity and carrier concentration in $\text{In}_2\text{O}_3\text{-SnO}_2$ compound.....		47
Fig.24.		
Resistivity Vs. Transmission in $\text{In}_2\text{O}_3\text{-SnO}_2$ compound.....		48
Fig.25.		
Hexagonal sheet of graphite to form a carbon nanotube.....		52
Fig.26.		
Zig-zag carbon bond (a) and Arm-chair carbon bond (b).....		52
Fig.27.		
(a)1-layered EL structure and (b) its cross sectional view of SEM.....		58
Fig.28.		
(a) 2-layered EL structure and (b) its cross sectional view of SEM.....		59

Fig.29. XRD patterns depending on the CNT concentration in ZnS:(Cu, Al).....	60
Fig.30. SEM images of CNT impurity doped ZnS:(Cu, Al).....	61
Fig.31. EL spectra of CNT free–ZnS:(Cu, Al) EL Device	62
Fig.32. EL spectra of CNT doped–ZnS:(Cu, Al) EL Device.....	63
Fig.33. Photograph of emitting EL device using a CNT doped–ZnS:(Cu, Al) phosphor	64
Fig.34. Critical voltages depending on BaTiO ₃ layer in TCO doped–ZnS: (Cu ,Al) EL device.....	65
Fig 35. EL intensity depending on the layered structure in ZnS:(Cu, Al) EL device.....	66
Fig.36. EL intensity depending on the applied voltages in ZnS:(Cu, Al) EL device.....	67
Fig.37. EL intensity of ZnS:(Cu, Al) layer depending on the inserted In ₂ O ₃ and SnO ₂	68
Fig.38. Compared EL intensities under 1–layer structure depending on the inserted In ₂ O ₃ and SnO ₂	69
Fig.39. Schematic showing electron flow under the 2 basic layered structure.....	70
Fig.40. Schematic showing electron flow under the 1 basic layered structure.....	73

ABSTRACT

This research focus to characterize luminescence properties related to Carbon Nano Tube (CNT) and Transparent Conductive Oxide (TCO) like In_2O_3 or SnO_2 being dispersedly inserted into ZnS-based EL device which are fabricated by screen printing method. More specifically X-ray, FE-SEM measurement and L-V (Luminescence vs. Voltage) are carried out to characterize electro-optical properties of ZnS-based Electro Luminescence (EL) devices depending on layered structures and material constitutions. Firstly, we confirmed that an optimum value of CNT concentration in the ZnS based EL device is about 0.75 atm. % resulting that the electric conductivity is 1.6 times higher than that of pure CNT sample. In addition, according to EL measurements, the enhance EL intensity with the dopant TCO like In_2O_3 or SnO_2 about 1 wt % insertion is approximately 1.2 times greater than that of TCO free samples. Clearly, CNT or TCO like conductive dopant material in EL device is presenting in the luminescence process providing a pathway for the creation of hot electron but overly inserted CNT may hinder to produce the hot electron. In case of the EL structure variation under the same condition, the 2 layered EL structure having a separate dielectric layer is more stable showing that its EL intensity is 1.4 greater than that of the 1 layered structure.

Keywords : Electro luminescence, Screen Printing, CNT, TCO

1. INTRODUCTION

Not only ZnS-based phosphor held an important place in the historical development of electroluminescence material, but it still leads prominently in current research theme, more specifically it attracts its importance as being a composites or a hybrid form in the field of panel electroluminescence[1–7]. Recently, as a cost effective way in the area of photovoltaic device, inorganic phosphor composites to fabricate the panel electroluminescence using various printing technologies on a suitable substrate have been widely studied in order to provide useful solution for the application areas of printed electronics [8–15].

Numerous research activities regarding Electroluminescence panel structure can be organized into three categories being characterized firstly, the dielectric behavior of thin film, secondly the interface phenomena between adjacent film layers, and finally the optical behavior of luminescence layer. Especially, due to the low efficiency of film phosphor, various efforts is associated to enhance the high output of luminescence intensity for the practical application[16–18]. On the other hand, CNT (carbon nano tubes) have been widely studied due to their typical characteristics in electrical (high conductivity : an order of a few micro ohm cm), thermal (high conductivity : 6600 W/m K) and mechanical properties[19–23].

Various composite materials having CNT element possess eventually both physical or chemical characteristics as a host material, and the inserted CNT element itself but sometimes reveals a unique property showing a new characteristic of composites due to the synergy effect from different species of combined elements[24,25]. In recent, CNT doped cathodoluminescent (CL) properties of the composites in CNT-ZnS (Cu, Al) phosphor shows enhanced luminescence characteristic and offer increased opportunity for further investigation for CNT as a promising doping material[26].

Also, TCO like In_2O_3 or SnO_2 material provide another possibility for enhancement of luminescence characteristic where doped solar cell device show excellent performance resulting in a high quantum efficiency. The typical characteristic of TCO material like In_2O_3 , ZnO , or SnO_2 is related to the transparent property in light (photon) pathway and conductive property in current (electron) pathway in simultaneous contrary to most transparent electric insulators which form oxide compound material. For an example, the TCO material a typical example of Indium Tin Oxide (ITO) thin film has a high transmission rate in visual wavelength range of light and high electric carrier concentration in simultaneous[27,28].

Referring our previous experimental results with the

electroluminescence properties of the screen printable thin film and the characteristics and behavior of CNT element in the phosphor composites, in this letter, the experimental results of photo and electro luminescence properties caused by CNT element in the phosphor composite film of CNT-ZnS:(Cu, Al) fabricated by a screen printing techniques will be interpreted.

Research activities concerning EL device structure can be classified into three categories being characterized. Firstly, the dielectric behavior of thin film, secondly the interface phenomena between adjacent film layers, and finally optical behavior of the luminescence layer. In case of thin film EL device using screen printing method, especially, due to the low efficiency, various efforts is focused to enhance high luminescence intensity and stable output to accomplish a practical EL device considering that all three research categories is closely related.

Recently, researchers and engineers have been renovating the printing technology as a new electronic manufacturing process because of the capabilities it offers that cannot be achieved by the vacuum based thin film fabrication process like Chemical Vapor Deposition (CVD) or Physical Vapor Deposition (PVD) methods for making thin film devices in electronics [29–33].

Screen printing method on the other hand is a promising

technology due to its low cost technique that has been used for years in mass producing two-dimensional low cost reproductions. This thin film fabrication method incorporates prototyping in production and allows the use of an almost limitless variety of materials as 'screen printable solutions'. Many companies have already commercialized “nano paste” products in OLED, photovoltaic device and electronic circuits etc. that also could enable to make EL devices as screen printable process providing printable phosphors and dielectric material in the field of inorganic EL display.

To design an EL device and to enhance electroluminescent performance, various requirements have to be satisfied by the thin layers and the interfaces between these layers. At the interface between the phosphor and dielectric layers, the designing of materials and structures are crucial to promote electric carrier injection and charge trapping in the interface.

Motivated by the promising results from composite dielectric layer contains a composite BaTiO₃- carbon nanotube (CNT) film, which is formed by adding CNTs into a BaTiO₃ layer in EL structure, the structural and luminescence properties of ZnS-based inorganic EL devices related to transparent conductive oxide (TCO) based on two different layered EL structures fabricated by screen printing

method are studied in this experiment.

In this research, the enhance luminescence results in ZnS-based EL device related to TCO material of In_2O_3 or SnO_2 mixed into the BaTiO_3 composites and the luminescence effect due to the formation of the separate buffer layer of BaTiO_3 are discussed with the interpretation of measured EL spectrums.



2. THEORY [34–36, 37–39]

Four mechanisms are involved in an thin film EL device to luminescence with applied alternating current. Firstly electrons from the interface states start tunnel emission. Secondly the tunnelled electrons are accelerated to high energies. Thirdly the accelerated electrons are collided with luminescence centers resulting impact ionization of the luminescent center, and Finally the de-excitation of the excited electron by emitting photon (radiative recombination) or non-radiative recombination providing phonon.

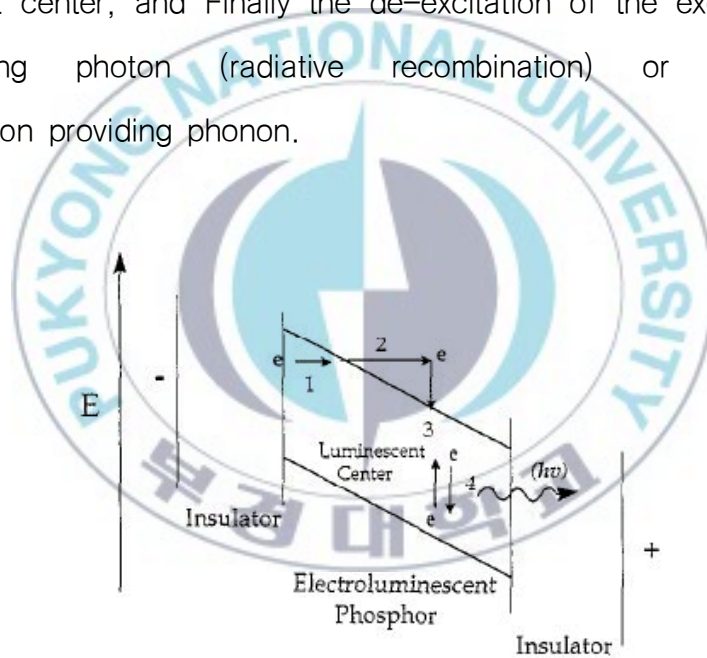


Fig.1 Electroluminescence process for AC thin film EL device

Referring the basic luminescence mechanisms, detail process and theory of AC thin film Electroluminescence device are worthwhile to discuss herein below.

2.1. Tunneling

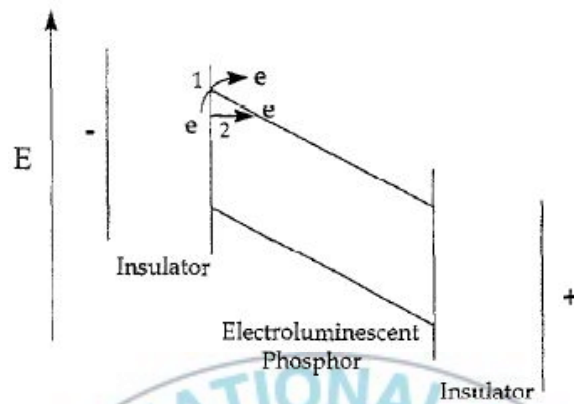


Fig.2 Energy band diagram showing the mechanism of two electron tunneling

Several experimental data are available that support the electrons trapped electrons at the interface between phosphor and insulator play as the carrier sources, and the tunnelling mechanism of injected electrons assisted by thermal excitation are responsible for their injection.

$$J \sim E^2 \exp \left[\frac{-8\pi\sqrt{2m^*}(q\Phi_B)^{3/2}}{3qhE} \right] \quad \text{---- (1)}$$

The tunnelling electron current density J for the schottky barrier will be given by above mentioned equation. Where E is the external electric field, m^* is the electron effective mass, q is the charge of an electron, Φ_B is the barrier height, and h is Planck's constant. The depth of

optimum electron trap is necessary to balance between two competing processes. If the electrons are too deep, the electron injection will not occur until extremely high fields are reached. In adverse, if the trapped electron are too shallow, electrons will inject at low fields and will not be accelerated to high enough kinetic energies to promote luminescence related to the electron-hole pair transition in phosphor material. Empirically, according to the various experimental data, electron state depths 1.0 ~ 1.3 eV have revealed in good device performance.

$$E_p = \frac{\epsilon_i}{\epsilon_i d_p + \epsilon_p (2)d_i} V_{tot} \quad \text{---- (2)}$$

Once the electrons are tunnel injected into the phosphor layer conduction band, the injected electrons are accelerated under the external electric field. The electric field in the phosphor layer can be calculated by rearranging Maxwell' equations applicable to the corresponding model of series capacitors. The resultant equation for the phosphor electric field E_p is the equation. Where ϵ is the dielectric constant, d is the layer thickness, and the subscripts i and p denote the insulator and the phosphor in electro-luminescence device respectively. For an example, if we are substituting typical value for $\epsilon_i = 20$, $d_i = 600$ nm and $\epsilon_p = 13$, $d_p = 500$ nm and the applied voltage $V_{tot} = 220$ V, then the phosphor electric field approximately E_p become 2.5 MV cm^{-1}

$$En_e(x) = E_p x \quad \text{--- (3)}$$

If one assumes loss-free electron transport, the electron energy $En_e(x)$ can be expressed as following equation. The electron energy as a function of distance (x) under an electric field E_v . Because electrons scatter and lose energy by several mechanisms, the electron energy distribution does not obey this simple relationship. The electron energy distribution would be a complicated function of scattering mechanism depending on the host phosphor and impurities related in the scattering center. For examples, Inter-valley scattering, polar optical phonon scattering, acoustic phonon scattering, ionized impurity scattering, band-to band impact ionization and impact excitation, these scattering mechanism closely depend on the energy band properties of the host phosphor.

2.2. Impact Excitation/Ionization

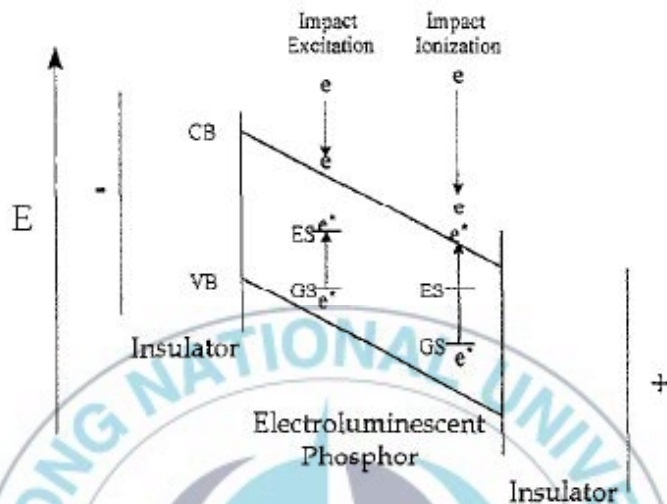


Fig.3 Mechanism showing the impact excitation and impact ionization

After the electrons accelerate to high enough energies, they can interact with a luminescence center in host phosphor and transfer the energies in order to excite from ground state (GS) to the excited state (ES) as shown above drawing.

The energy transfer to higher atomic state from acceptor impurity level to donor impurity level is called impact excitation while the energy excitation into the conduction band of host material is called impact ionization. The probability of electron luminescence center interaction is proportional to the luminescence center radiative cross-section. When the electron is excited into a higher atomic state, it can relax back into its

ground state either radiative (photon related emission) or non-radiative (phonon related emission).

When an electron is promoted into the conduction band (impact ionization), the excited electron is immediately accelerated toward the anode by the applied electric field. This type of impact mechanism causes electron multiplication in host phosphor and is referred to this phenomena as avalanche breakdown.

2.3. De-Excitation : radiative or non-radiative recombination

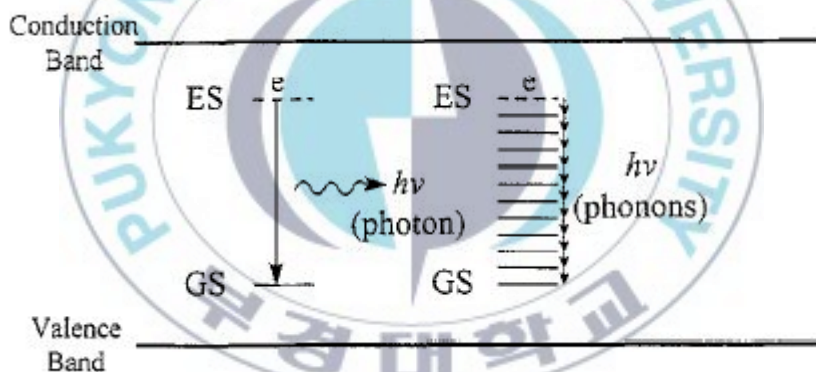


Fig.4 Energy diagram showing a radiative and a non-radiative de-excitation path

De-excitation process can occur either radiative (which produce a photon) or non-radiative. Non-radiative relaxation occurs by phonon generation which produce heat from lattice vibration. The above mentioned schematic figure show that these two relaxation processes

respectively. Local lattice imperfections such as interstitial lattice defect, lattice vacancies, line defects like dislocation of lattice or volume defect like grain boundaries are also act as non-radiative recombination center which deleterious to the radiative efficiency.

The radiative efficiency as a function of temperature $\eta(T)$ is written as following equation.

$$\eta(T) = \frac{I}{I(0)} = \frac{W_R}{W_R + W_{NR}} \quad \text{-----} \quad (4)$$

where W_R , W_{NR} are the radiative and non-radiative recombination rates respectively. Furthermore W_{NR} is given by the temperature dependent expression.

$$W_{NR}(T) = W(0) \exp \frac{-E}{kT} \quad \text{-----} \quad (5)$$

where $W(0)$ is the order of the lattice vibrational frequency, E is the activation energy, k is Boltzmann's constant and T is temperature. From these equations, we can see the non-radiative recombination rate increase with temperature while the radiative recombination rate is temperature independent. Subsequently, the radiative recombination rates related to the luminescence decrease as the temperature increase due to an increase in non-radiative recombination rate with a phonon generation

caused by lattice vibration.

2.4. Radiative recombination

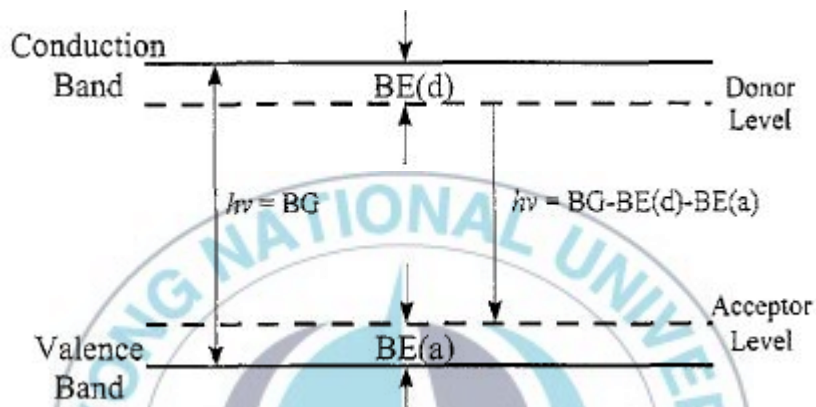


Fig.5 Energy band diagram showing Donor-Acceptor (DA) pair transition

The radiative recombination process of energy band diagram ZnS phosphor is schematically denoted as seen on the above. Under EL excitation, a large electric field is induced across the phosphor layer. When electrons are excited by the external electric field source into the Conduction Band (CB) and holes are created in the Valence Band (CV)

$$h\nu = BG - BE(d) - BE(a) \quad \text{-----} \quad (6)$$

BG is the semiconductor bandgap, BE(a) and BE(d) are acceptor and donor binding energies, respectively and $h\nu$ is the photon emission

energy of radiative recombination. When electrons and holes are trapped in close proximity to one another, this electron and hole (e-h) pair recombination is favorable and provide very high efficient result.

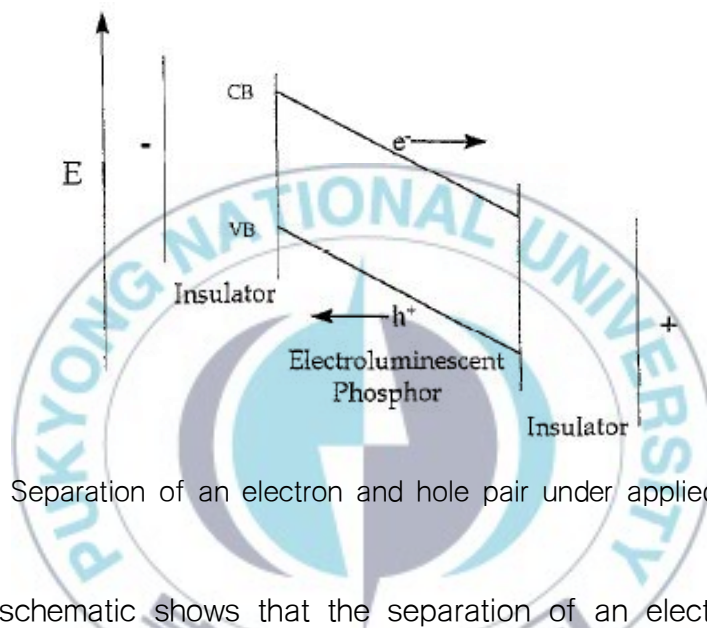


Fig.6 Separation of an electron and hole pair under applied voltage

The schematic shows that the separation of an electron and hole pair under the electric field bias. The electron move toward the positive polarity (anode) and the hole move towards the negative polarity (cathode). In case of high external fields there is a low probability and low cross section to create for trapping electrons and holes at the donor and acceptor sites. Although electron or hole is trapped by the donor and acceptor level, the decay time is long enough and the depth of these levels relatively shallow enough under the strong electric external field bias so that electron and hole are tunnel back into the CB or VB

before they make electron – hole radiative recombination.

2.5. Luminescence center and the atomic transition

The luminescence center dominates the optical emission properties of the phosphor layer. When discussing the luminescence center, three aspects must be considered, namely the radiative kinetics, the cross-section for excitation, and the radiative transition energy. Especially, the cross-section for excitation is important to characterize the optical emission in phosphor layer. The excitation cross-section is related to the probability that a high energy electron will impact and excite or ionize luminescence center in the phosphor material. The excitation cross-section is proportional to the geometric cross section of the ionized luminescence center when the impurities substitute the site of host material.

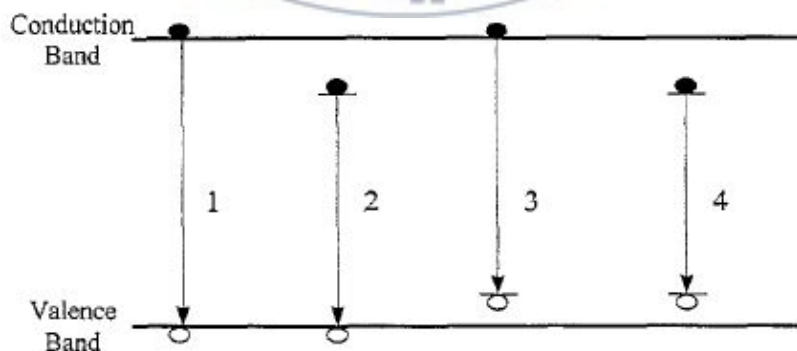


Fig.7 Schematic showing electron-hole recombination mechanisms

The above denoted diagram is showing four types of radiative kinetics related to the electron-hole recombination mechanisms. namely (1) band to band, (2) donor state to valence band, (3) conduction band to acceptor state, and (4) donor state to acceptor state recombination.

$$\eta = \frac{h\nu\sigma N}{eE} \quad \text{-----} \quad (7)$$

The power efficiency (η) of the EL device is directly proportional to the cross section of the luminescence center. $h\nu$ is photon energy and σ is the cross sectional excitation and N is the optimum luminescence center e is the charge of an electron and E is the electric field. As seen on the equation a large cross-section is desirable for efficient EL devices.

The probability of an optical transition (absorption or emission) is a function of the initial state and final state wavelength (frequency) and is denoted by the oscillator function as the below wavefunction equation.

$$f = \frac{8\pi^2 mc}{3he} G\nu M^2 \quad \text{-----} \quad (8)$$

where m is the electron mass, c is the speed of light, h is Plack's constant, e is the charge of an electron, ν is the frequency G is a

parameter which relates to the degeneracy of the transition and M is the transition moment.

$$M^2 = M_x^2 + M_y^2 + M_z^2 \quad \text{-----} \quad (9)$$

Where

$$M_x = \int \psi_m^* \sum e_i x_i \psi_n \, d\tau \quad \text{-----} \quad (10)$$

ψ_m^* is the wavefunction of the final state $\sum e_i x_i$ is x component of dipole ψ_n is the wavefunction of the initial state. The expression for M_y and M_z is similar to M_x . The equation demonstrates the origin of one of the optical transition selection rules under the quantum mechanics of Shrodinger equation.

The transition moment function must even because upon inversion, an odd function changes sign. To make the entire function is even, the wavefunction of the initial state or final state must be even and the other wave function must be odd. The result of this is so called the selection rule in angular momentum as shown the below.

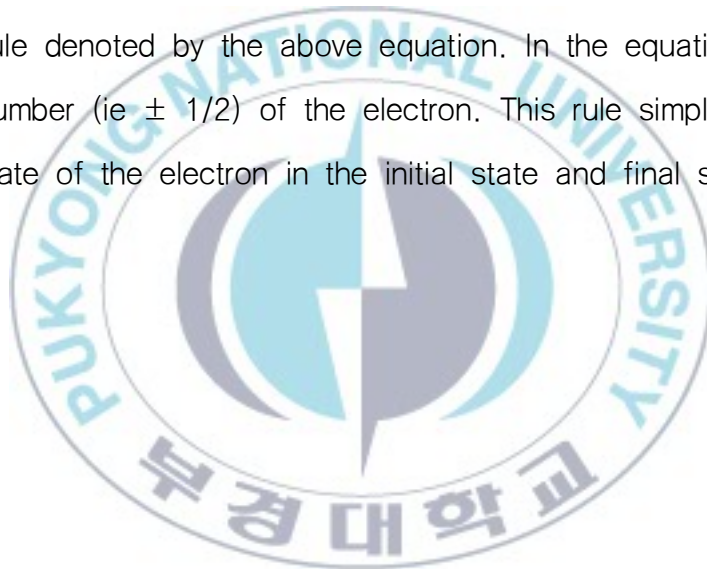
$$\Delta l = \pm 1 \quad \text{-----} \quad (11)$$

Δl is the change in angular momentum quantum number. For an electric dipole transition to be allowed, the angular momentum quantum number

must change by factor of the absolute value of 1. That means that the intra-shell transition like d-d, f-f, ... is forbidden because $\Delta l=0$ and certain transition like s-p, p-d, d-f ... are allowed because the transition satisfy the selection rule of $\Delta l= \pm 1$.

$$\Delta s=0 \quad \text{-----} \quad (12)$$

The second selection rule for optical transitions is called the spin selection rule denoted by the above equation. In the equation, s is spin quantum number (ie $\pm 1/2$) of the electron. This rule simply means that the spin state of the electron in the initial state and final state must be the same.



2.6. Host material and luminescence center interaction

The shape and symmetry of the d-orbitals have five orientation : the d_{xy} , d_{yz} , and d_{xz} each shape and symmetry have the same distribution, and the d_z^2 and $d_{x^2-y^2}$ each have unique distribution. The energy level position related to the each orientation depends on the location of neighboring anions.

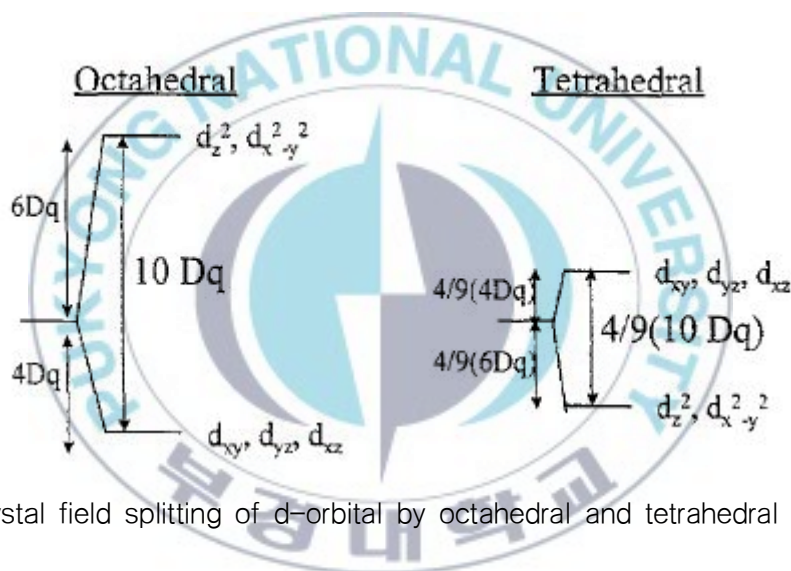


Fig.8 Crystal field splitting of d-orbital by octahedral and tetrahedral symmetry

Two basic types of crystal symmetries are important. Octahedral symmetry (sodium chloride structure) and Tetrahedral symmetry (zinc blend structure) Above denoted figure shows that the d-orbital splitting for both the octahedral and tetrahedral crystal field symmetry ignoring spin-orbit splitting.

Simple geometric considerations show that the d-orbital crystal

field splitting (Δ) of the tetrahedral symmetry is 4/9 of the magnitude of the octahedral splitting resulting that $\Delta_{\text{tet}} = 4/9\Delta_{\text{oct}}$

$$Dq = \frac{1}{6}ze^2 \frac{r^4}{a^5} \quad \text{-----} \quad (13)$$

Dq is a measure of the energy level separation, z is the charge or valence of the anion, e is the charge of an electron, r is the radius of the d wavefunction, and a is bond length. The above equation reveals that the emission of color can be changed depending on the lattice of space distance in the host material when a radiative transition occurs an outer d-orbital (3d or 5d). The magnitude of the d-orbital splitting for octahedral symmetry is given by $10 Dq$, and tetrahedral symmetry is given by 4/9 of $10Dq$ when the geometric symmetry of the cation site is considered as shown on the figure.

3. LITERATURE REVIEW

3-1. Screen printing technology for thin film

3.1.1. Screen printing process [14]

The schematic screen printing process illustrated in above figure shows pastes are released from meshes and are flowing together on the substrate.

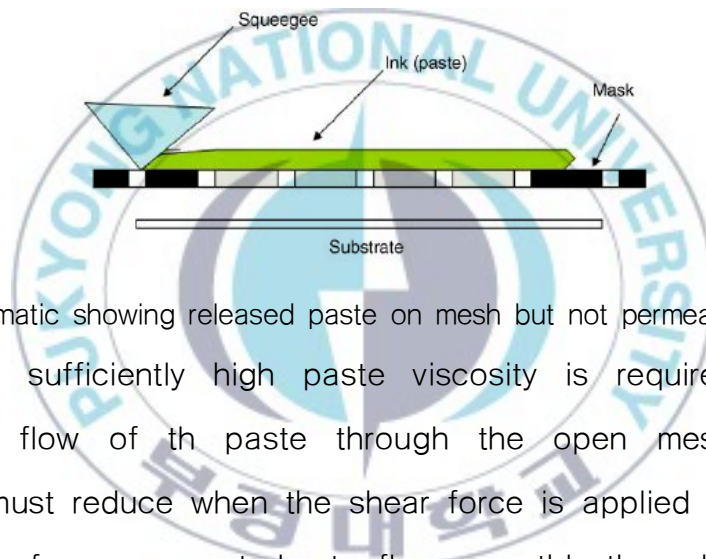


Fig.9 Schematic showing released paste on mesh but not permeable into mesh Initially, a sufficiently high paste viscosity is required to avoid premature flow of the paste through the open mesh. But the viscosity must reduce when the shear force is applied to the paste by means of squeegee stroke to flow smoothly through the screen mesh.

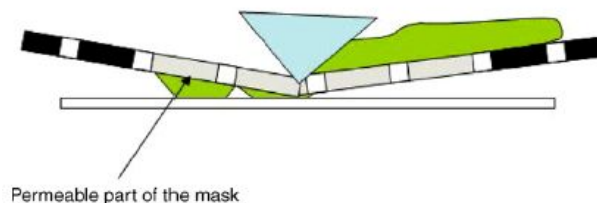


Fig.10 Schematic showing permeable part of paste by squeegee stroke

After printing, the paste must obtain its original viscosity with a short time delay to allow it to flow together in order to form an proper surface morphology preserving the printing pattern in the long term.

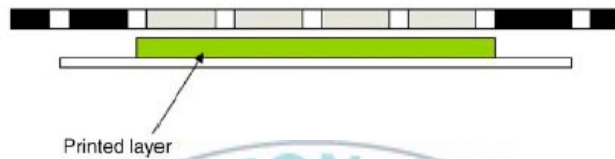


Fig.11 Schematic showing printed layer after finishing squeegee stroke

As shown on the above figure, the screen printing patterns are printed after the snap-off between the screen and the substrate. The sequence of C and D at which the paste is separated and transferred from the screen to the substrate are most critical points

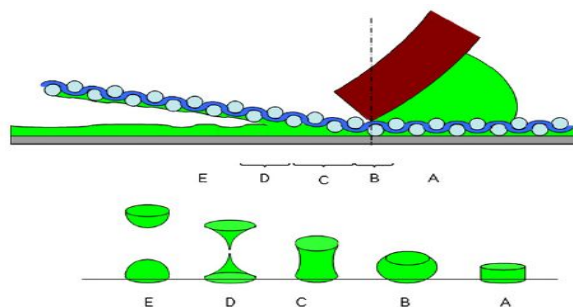


Fig.12 Schematic showing the paste separation from screen to substrate

Therefore, it is most important the snap-off speed should be kept in a constant speed to get the uniform patterns in the substrate. There are many other printing parameters to determine screen printable patterns such as printing pressure or squeegee pressure, screen mesh size, snap-off distance, rheological behaviour of paste and deformation characteristic of screen mesh.

3.1.2. Deformation in the screen mesh [40]

The parallel directional deformation of the screen mesh (ΔL) respect to the squeezing direction can be defined as follows

$$\Delta L = L_1 - L_0 = c + d - L_0 \sqrt{x^2 + h^2} + \sqrt{(L_0 - x)^2 + h^2} - L_0, \quad \text{----- (14)}$$

where L_1 is the deformed length L_0 is the original length of screen mesh and x is the displacement squeegee and finally h is off-contact length or snap-off distance as shown the below figure.

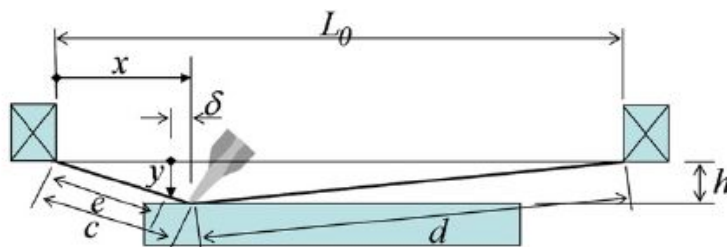


Fig.13 Length side view showing the deformation of screen mesh

For an example, in case of L_0 is 2000 mm and the effective screen printing range is 400 mm to 1600 mm, if the snap-off distance h is 1 mm, 2mm, and 5 mm then the maximum deformation of the screen mesh would be $0.56\mu\text{m}$, $2.3\mu\text{m}$ and $14\mu\text{m}$ respectively.

$$\Delta w = w_1 - w_0 = 2f + w_s - w_0 = 2\sqrt{\left\{\frac{(w_0 - w_s)}{2}\right\}^2 + h^2} + w_s - w_0, \quad \text{---- (15)}$$

The width deformation of the screen mesh (Δw) with respect to the direction of squeeze is expressed as the below equation.



Fig.14 Width side view showing the deformation of screen mesh

where w_1 is the deformed width, w_0 is the original width of the screen mesh w_s is squeegee width, and h is off-contact length or snap-off distance. If the original width of screen mesh w_0 is 1800mm and squeegee width w_s is 1200mm and the off-contact distance is 1 mm, 2mm and 5 mm then the width deformation of

screen mesh become $3.3\mu\text{m}$, $13\mu\text{m}$, and $83\mu\text{m}$ respectively according to the equation.

3.2. Application Industry of printing technology [8–15]

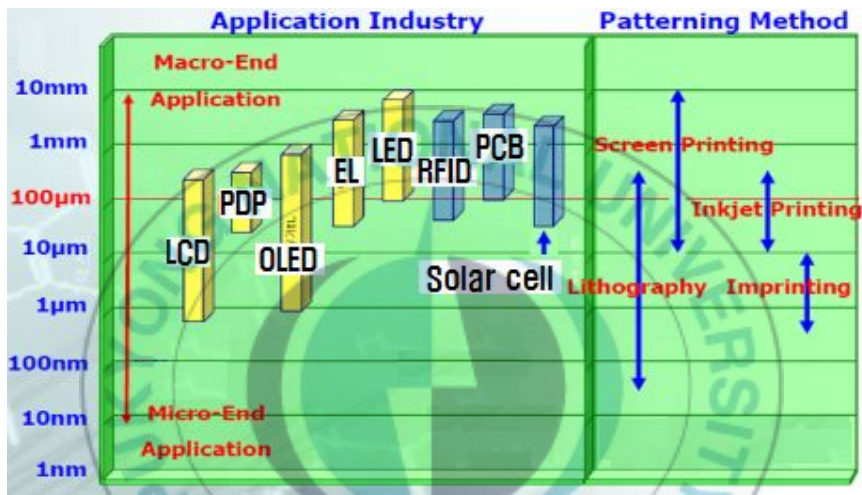


Fig.15 Schematic illustrating patterning thickness for printed electronic industry

The advantage in printing as a means of realizing electronic systems is primarily driven by the fact that printing technique is expected to be a low-cost technique for mass production of electronic device. To validate this advantage, it is worthwhile to compare printing-based fabrication to traditional micro-electronic fabrication techniques. First, printing method has been claimed to be cheaper than lithography based fabrication due to a lower

capital expenditure. Furthermore printing technique are no necessary for vacuum environment or relating facilities which needs more expensive cost for the device fabrication.

In fact, this is not accurate approach for the line width $< 10 \mu\text{m}$, since highly accurate lithographic tools are available in this regime. Additionally, to realize high end product for the solution of printed electronics, low defect printing tooling will necessitate the development of new equipment for printed electronics, adding to capital expenditure for the same amount in the traditional electronics technology.

Therefore, it is not clear that printing technology will reduce the capital expenditure in the electronic industry and expected to reduce overall process complexity, since it can enable the use of entirely additive processing, rather than necessitating the use of lithography+etch based subtractive processing.

However over the line width $> 10 \mu\text{m}$, the printing technique is a tremendous advantage, since it reduces the step count in overall process, raw material costs, and overall tooling cost, therefore reducing capital expenditure and increasing throughput across the entire production flow. Moreover, printing technique can potentially enable low-cost substrate handling and factory automation, since it allows the mass productive use of low cost

roll-to-roll or sheet-feed printing processing technique.

While this is likely a true fact in the long run, the development of high accuracy solutions for printing technology is still pending, and, as a result, the final outcome for the printable electronics is still unclear. By reviewing material costs, substrate costs, capital expenditure estimates, and throughput estimates, it is possible to draw a broad conclusion regarding the economic viability and the road map of printed electronics.

Overall analysis on the reviewing factors suggests that printing technique should potentially be cheaper per unit area than conventional electronics. The actual cost advantages depend on the specific printing process flows used, but cost advantages over 10 times per unit area appear quite feasible. On the other hand, the cost per transistor in printed electronics is several orders of magnitude higher than the cost per transistor in silicon, due to the much worse line width (the best achievable the line width in high-speed printing technique today is about 10 μm).

As a consequence, the economic comparison can be summarized in various applications that are limited depending on the area-constrained by the line accuracy. As seen on the figure 15, various printing techniques are available to be used in the fabrication of electronics depending on the line thickness. Screen

printing has the line width $10\mu\text{m} \sim 10\text{ mm}$ while ink-jet printing has the patterning width between $10\mu\text{m}$ and the less size of 1mm . The more useful printing technique is imprinting method to cover the line width below than $1\ \mu\text{m}$.

It is therefore worthwhile to summarize the advantages and disadvantages in connection with each of the broad classes of printing techniques. The printing techniques that will broadly be included here are screen printing, inkjet printing, stamping / nano-imprinting, and gravure printing. Other printing techniques do exist, but have generally not been applied to printed electronics fabrication.

Screen printing is arguably the most mature technique for fabrication of printed electronics. Screen printing has been applied to the fabrication of printed circuit boards for decades. In screen printing, a viscous ink is pressed through a patterned screen using a squeegee. The pattern on the screen is typically generated using a photosensitive screen coating.

Screen printing is widely use in printed circuit boards, since it can be used to pattern conductor traces typically using silver pastes, to pattern resistors using carbon films, to fabricate capacitors using polyimide dielectrics etc. for the application of printed electronics. The resolution of commercial high-speed screen

printing tools is typically limited line width of $50\mu\text{m}$, although in research, screen technology has been applied to realize prints in the range of $< 10\mu\text{m}$.

The main disadvantage of screen printing relates to the viscosity of the ink. Since the ink is forced through a screen and is therefore free standing when it lands on the substrate, inks with relatively high viscosity (typically > 1000 cP) are required to prevent excessive spreading and bleed out.

This is problematic for some materials in printed electronics. High viscosity inks are typically realized by adding polymer binders to the ink. While this is not a problem for graphic arts but it can be a serious problem for printed electronics, since such binders can destroy the functionality of semiconductors, introduce excessive leakage and dissipation in dielectrics or degrade the conductivity of conductors.

As a result, the use of screen printing is typically limited to applications where binders can be added without unacceptable loss of performance. For example, binder laden silver pastes are commonly screen printed. While the conductivity is degraded relatively to pure thin film silver, it is still acceptable for the target applications (e.g., thin film membrane switches, automotive keypads, etc.). Screen printing has been used in some limited

applications for printed electronics such as printing interconnection.

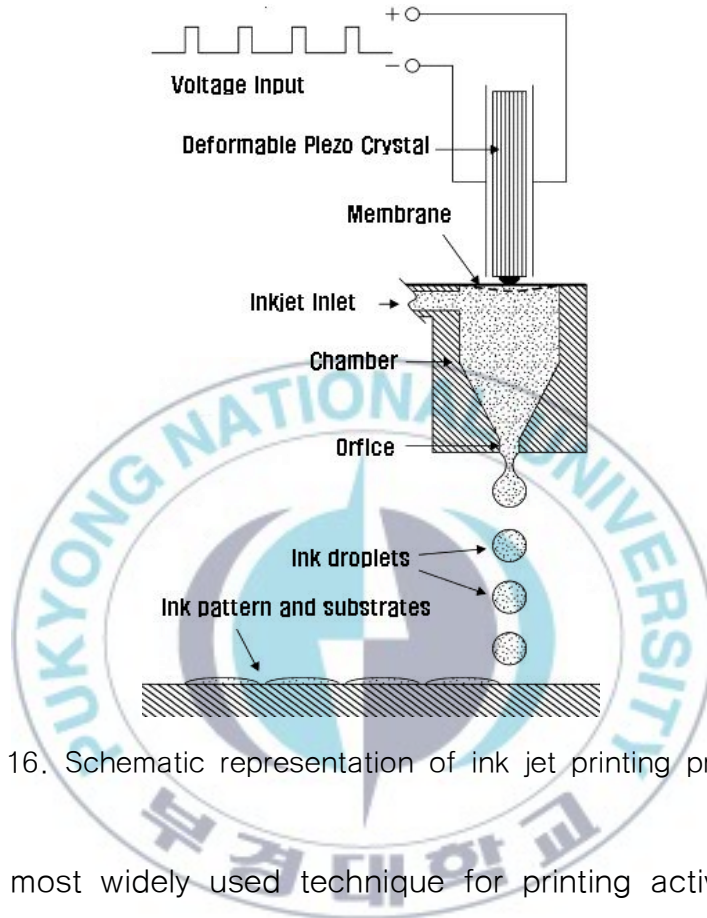


Fig. 16. Schematic representation of ink jet printing process.

The most widely used technique for printing active electronic circuits today is inkjet printing. Inkjet printing allows the use of low viscosity inks (1–20cP); this is extremely important, since it allows for the formulation of inks that only contain active material and solvents without the need for binders. Coupled with digital input, which allows for on-the-fly design changes, inkjet printing dominates research into printed transistors, etc. On the other hand,

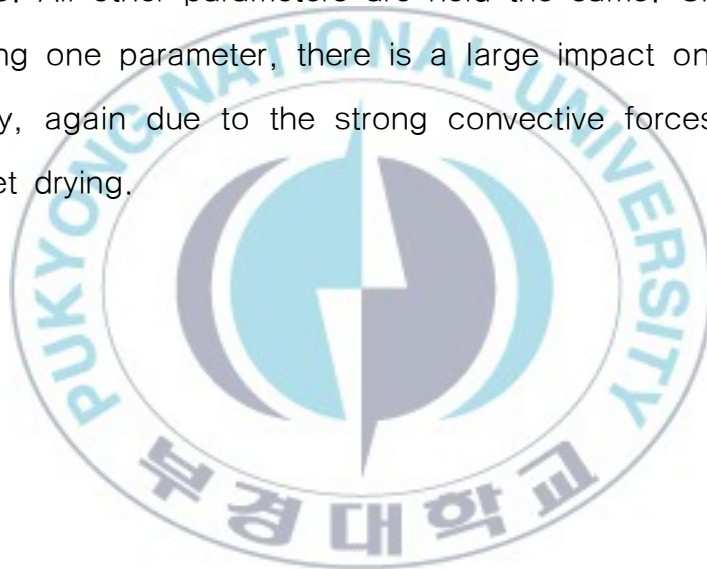
the manufacturing viability of inkjet printing is still unclear.

First, inkjet printing, being a drop-by-drop technique, is prone to severe pixilation-related issues, where the complex drying phenomena associated with droplets can produce widely variant printed patterns. This will be discussed further below. Second, inkjet printing tends to be slow, and high throughput is only achieved by using large numbers of heads in parallel. This in turn introduced yield concerns related to the misfiring of individual heads during printing of a pattern. Third, there is a cone of uncertainty associated with the ejection angle of drops from a nozzle ; this typically results in a $\pm 3\sigma$ variance in placement of the drop of up to 10 μm . This in turn introduces line edge roughness and places limits on design rule scaling.

The drying phenomena associated with inkjet printing are particularly important, since smooth, thin films with low line edge roughness are typically very important for the realization of printed devices. Inherent to the drying of drops is the so called “coffee ring effect”. In this effect, as drops dry, there is strong migration of material from the center of the drop towards the edges of the drop due to strong convective forces associated with solvent evaporation from the drop.

Depending on the relatively evaporative and convective

fluxes, as the drop dries, it is possible for a donut shaped final film to result. This is obviously a serious concern for printed electronics, since the large thickness variation, inherent presence of pinholes, and sharp ridges all contribute to unacceptable film formation. The impact of drying on line formation is clearly visible variation in line morphology as a function of drop spacing in a printed line. All other parameters are held the same. Clearly, simply by changing one parameter, there is a large impact on printed line morphology, again due to the strong convective forces associated with droplet drying.



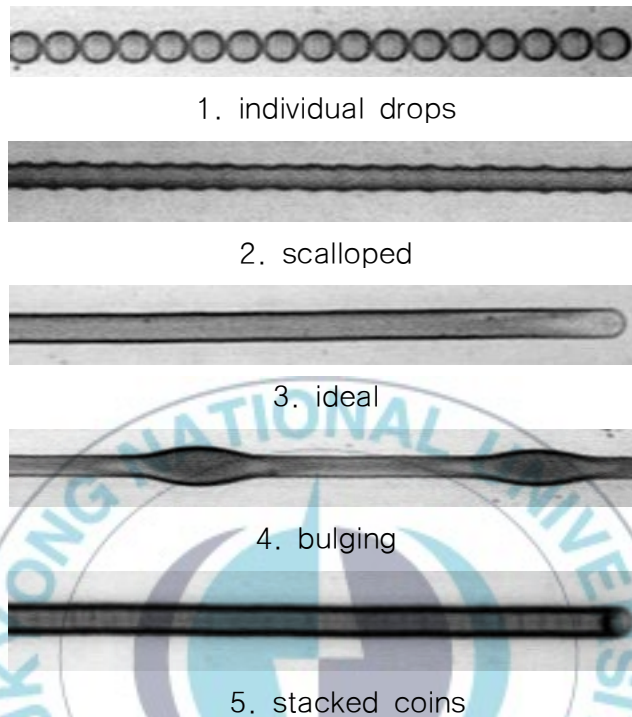


Fig. 17. Effect of droplet spacing on final printed line morphology

The origin of the printed line variations above is easily understood by considering the convective forces associated with drying. As a drop is appended to the end of an already formed line, convective forces cause the fluid within the drop to flow towards the connection point to the line. If the drop-spacing is too wide, then this connection is too small to support the flow, resulting in the drop drying before a continuous line is formed (Figure 17.1). If the spacing is slightly closer, then some material

flows into the line, but the narrow connection constricts flow, resulting in the drop drying / gelling before a smooth sidewall is formed, resulting in scalloped lines (Figure 17.2).

If the drop spacing is reduced further, then smooth continuous lines can in fact be formed (Figure 17.3). However, should the drop spacing be reduced further still, then the connection point between the drop and the line gets too large, and excessive material from the drop flows into the line. The line is unable to support this flow, and therefore, the line pools up, producing a bulge. The increased cross-section of the bulge allows further absorption of fluid and thus the bulge necks back down again, only to increase when the impedance to fluid flow builds back up again. This results in the formation of periodic bulges in the line (Figure 17.4).

It is clear, therefore, that line morphology control is complicated, and the manufacturability of the same is therefore challenging. A brute force solution that is commonly adopted by numerous authors involves “flash drying” the line such that drops dry very rapidly upon hitting the substrate. This forms lines composed of overlapping individually dried drops (Figure 17.5). Unfortunately, such lines suffer from poor thickness uniformity, limiting film and feature scalability.

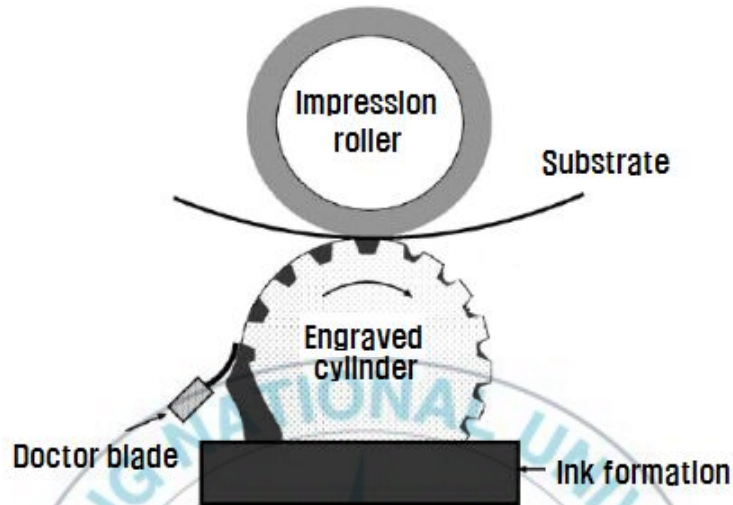


Fig. 18. Schematic representation of gravure printing process.

The pixilated nature of inkjet printing and its low throughput and manufacturing challenges have driven interest in alternative printing technologies. The big concern, of course, is viscosity; the next lowest printing technique in terms of viscosity requirements is gravure printing, and indeed, there has been substantial interest in gravure printing for printed electronics in recent years. In gravure printing, a drum with features (cells) etched into it is inked and wiped with a doctor blade to remove ink from field regions. This drum is then rolled over the substrate to be printed. Some fraction of the ink in the wells transfers to the substrate, resulting in printed patterns. The advantage of gravure printing is that it is very

high speed, and is scalable to produce patterns below $20\mu\text{m}$ with excellent pattern fidelity, including good film uniformity and low line edge roughness.

The disadvantages of gravure include the fact that it is a contact technique, and therefore has significant defectivity challenges, and that it requires higher viscosity inks (typically $40\text{ cP} \sim 2000\text{ cP}$). As a result, it is relatively unstudied for printed electronics, but has gained attention in recent years. As with inkjet printing, the stringent line edge morphology and surface roughness requirements of printed electronics have implications on the use of gravure printing. Since gravure printing involves the inking and subsequent de-inking of the wells on the gravure cylinder, the optimization of these processes must be considered very carefully.

For example, during de-inking, there are strong lateral shear forces, and improper optimization of the process can result in pickout, in which ink is “pulled” off the printed pattern. In gravure, the printed pattern depends strongly on the cell structure. By varying the cell height and width it is therefore possible to tune the printed feature size. Gravure has the advantage of allowing printing of films with a wide range of thicknesses, from $50\text{nm} \sim 5\mu\text{m}$, while also allowing good scalability of linewidth, to below $20\mu\text{m}$.

The final printing techniques that are being pursued are

stamping and nano-imprinting. These are similar to gravure printing, in that a patterned master is used to transfer a pattern onto a substrate. In stamping, the master is inked and pressed on the substrate, while in nano-imprinting, the substrate is inked and the master is pressed into it. Both techniques have shown good results in research, though it is too early to comment on their manufacturability.

Overall, it is likely that printed electronics will ultimately make use of many of the above. For different layers, different printing techniques will be optimal, based on pattern requirements and material compatibility. Therefore, a mix and match approach will be used, with the goal of maximizing process throughput for a given capital expenditure.

By examining the devices and economic considerations above, it is possible to draw certain conclusion regarding the best uses of printed electronics:

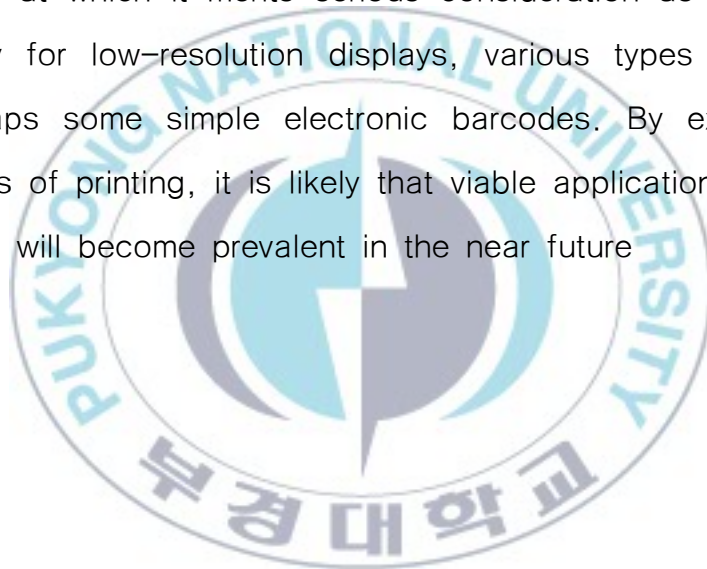
First, printed electronics is economically attractive in applications that are area-constrained, rather than functional density constrained. Displays are therefore an obvious application. Other applications include some types of sensors (the functional density of a sensor is often dominated by the size and form-factor of the sensing element) and RFID tags operating at relatively low

frequencies, such that the size of the antenna and passive components dominate the overall size of the tag.

Second, printing in general and inkjet printing in particular allows for the relatively easy integration of mutually incompatible and diverse materials on the same substrate. Therefore, applications that require diverse materials functionality are often attractive for printed electronics. Again, various types of sensors are obvious candidates, as are tags incorporating a range of functions including communication, sensing, visualization, etc.

Third, the performance of printed electronic devices will generally be relatively poor, particularly for electronics on plastic. Due to the low-temperature processes, lack of self alignment, poor film quality, large line width, and lower performance materials used, transistors fabricated for printed electronics will typically operate at frequencies below 1MHz, and will be relatively large. This limits the use of printed electronics to applications that do not require large numbers of transistors or high performance. Again, obvious examples are displays, some simple sensing circuits, and perhaps some simple electronic barcodes. At this point, therefore, it is appropriate to review some of the major applications of printed electronics on a case-by-case basis, identified the advantages and tradeoffs therein.

Printed electronics is an attractive technology for realizing electronic systems on flexible substrates. Economic considerations suggest that printed electronics may be advantageous for systems requiring large areas or low functional densities, such as displays, sensors, and some RFID tags. While the performance of printed transistors is generally poor, it is improving rapidly, and is already at a point at which it merits serious consideration as a candidate technology for low-resolution displays, various types of sensors, and perhaps some simple electronic barcodes. By exploiting the advantages of printing, it is likely that viable applications of printed electronics will become prevalent in the near future



3.3. Electroluminescence ZnS based thin film [4–7, 18]

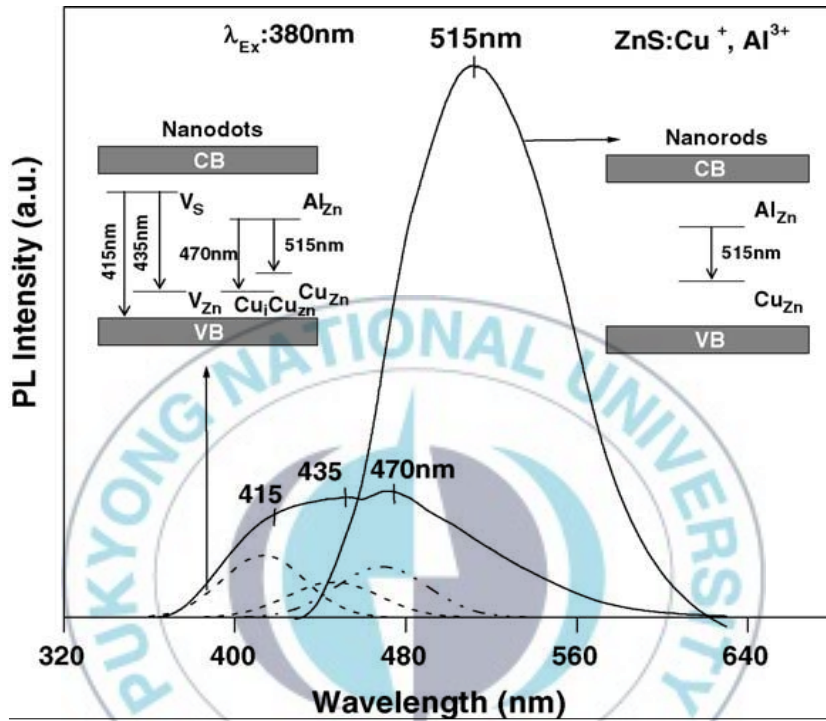


Fig.19. Photoluminescence characteristics of ZnS:(Cu, Al) pure phosphor

The high-energy side bands (415 and 435 nm) are attributed to the presence of a large concentration of lattice vacancy centers such as V_S and V_{Zn} in the nanoparticles, whereas the emission at 470 nm is attributed to a donor-acceptor (D-A) type electronic transition involving Al_{Zn} and Cu_iCu_{Zn} . Relatively comparable emission intensities of both the defect as well as dopant related emission bands indicate that the defect centers are highly competitive in nature. However, it is interesting to see that, when the same

nanoparticles begin to self-assemble and grow into nanorod geometries, the intensity of the blue side bands is reduced significantly while the intensity of green emission at 515 nm increases remarkably. This green emission is attributed to donor-acceptor type recombination between aluminium (Al_{Zn}) and copper (Cu_{Zn}) centers situated substitutionally at the Zn^{2+} site.

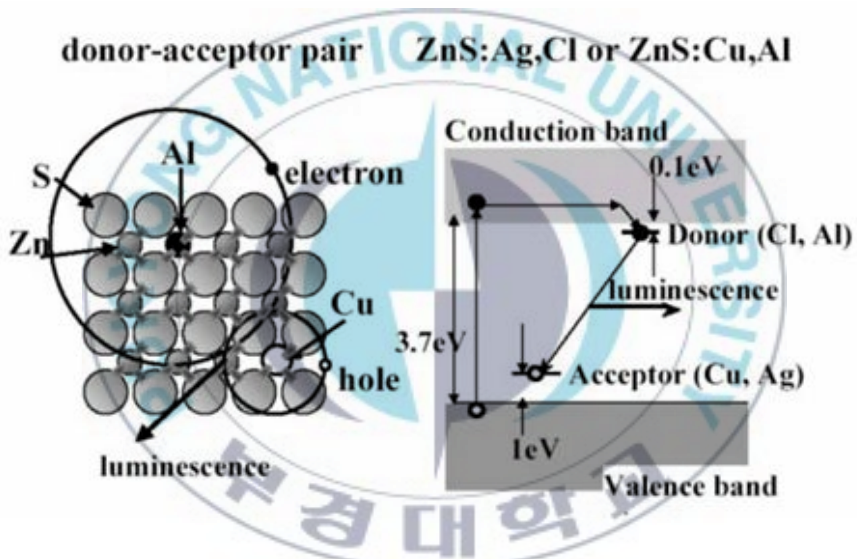


Fig.20 Energy band gap diagram of ZnS:(Cu, Al) phosphor

These results indicate that the vacancy centers are annihilated during the particle-to-particle attachments, which in turn increase the efficiency of the dopant related emission process. Further, the observed red shift in the peak maximum of the copper-related emission from 470 nm in nanodots to 515 nm in nanorods suggests that the nature of the luminescent centers is

dynamically modified during the self-assembly process. The energy-band diagram in Fig.19 schematically illustrates the difference in the radiative transitions in nanodots and nanorods.

The phosphor powder ZnS are made by grinding naturally grown crystal so that the average size of powder particle is a few microns. These particles are embedded in dielectric layer (insulator) in varying concentration and sandwiched between the transparent electrode and silver electrode to fabricate an electroluminescence device. Single grain of phosphor or small groups of grains are completely enclosed by dielectric material.

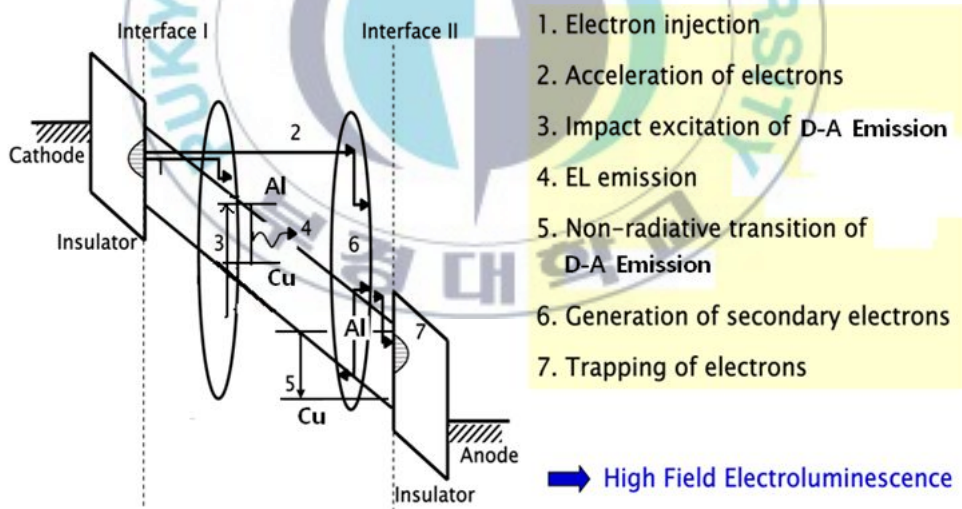


Fig.21 Electroluminescence mechanism of ZnS:(Cu, Al)

The basic mechanisms leading to local bistability, and thereby

to the formation of filamentary domains in thin-film ZnS:(Cu, Al) EL devices, can be described qualitatively in the following sequence:

(1) conduction is initiated by the tunnel injection of electrons from the insulator-ZnS interface;

(2) the electrons are accelerated by the high (10^6 V/cm) electric fields in the active layer, leading to impact excitation of Mn activator centers and impact ionization of the ZnS host, i.e., the creation of electron-hole pairs;

(3) some of the holes so produced are captured in deep traps, thereby inducing a space charge and a subsequent distortion of the electric field;

(4) the expected reduction of the tunnel injection resulting from the voltage quenching due to the flow of charge to the interfaces is offset by the distortion of the electric field, thereby allowing additional current to flow;

(5) when finally there is a reversal of applied voltage, the charge which has collected at the ZnS-dielectric interfaces adds to the internal electric field applied to the active layer, leading to a further enhancement of current flow and space-charge generation, such that flow is maintained even with subsequent reduction in applied voltage below the threshold voltage;

(6) with further reduction in applied voltage, the progressive

elimination of space charge by the recombination of injected electrons with the trapped holes exceeds the generation rate of new space charge, and the process reverses, culminating in a state where there is little space charge and little injection current.

3.4. Material properties of transparent conducting oxides (TCO)

[24–28, 41–45]

In definition, the typical characteristic of TCO material like In_2O_3 , ZnO , or SnO_2 is related to the transparent property in light (photon) pathway and conductive property in current (electron) pathway in simultaneous contrary to most transparent electric insulators which form oxide compound material. For an example, the TCO material a typical example of Indium Tin Oxide (ITO) thin film has a high transmission rate in visual wavelength range of light and high electric carrier concentration in simultaneous. Typical characteristic of the electric conduction (σ) in TCO is less than $10^3 \sim 5 \text{ } [\Omega\text{cm}]^{-1}$

$$\sigma = e \mu N \text{ } [\Omega\text{cm}]^{-1} \quad \text{----- (16)}$$

where e is the constant of electron charge, μ is the charge carrier mobility and N is the charge carrier concentration case of thin film formation, TCO's sheet resistivity (R) should be less than $10^{-3}\Omega$

$$R=1/(\sigma d) \quad \text{----- (17)}$$

where σ is electric conduction and d is the thickness of thin film

$$\varepsilon = (8\varepsilon_0\omega/\sigma) = 1 - RIR \quad \text{----- (18)}$$

The above mentioned equation shows that the light emissivity (or permittivity) of TCO. where ε_0 is permittivity of vacuum, ω is the angular frequency of incident light, and σ is electric conduction. RIR is reflectivity of thin film. For a example, a blackbody's emissivity is 1 corresponding RIR is 0 which totally absorbs the light energy.

The TCO material like In_2O_3 , ZnO , or SnO_2 reveals following common properties in usual. The material has a wide band gap energy of the over 3.3 eV which is larger than that of the energy band gap of visual light resulting that no absorption in the visual wavelength of light. Those are n-type conduction material and their binding force with a glass material (SiO_2) is strong resulting the suitable coating material for making transparent substrate in various field of industry. In addition, those materials are also relatively stable and strong with respect to external chemical treatment or mechanical scratch.

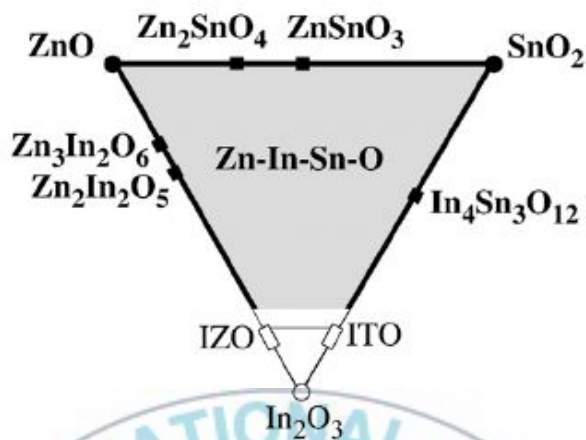


Fig.22 Example of useful TCO compound material

In recent, active researches on the thin film compound related to TCO are carried out to find optimum concentration varying the material composition of binary compound In₂O₃, ZnO, and SnO₂ as shown on the above figure. Multi-component oxides can be derived using the combination of these binary compounds of In₂O₃, ZnO, or SnO₂. The multi-component oxides like ZnO-In₂O₃ (IZO), In₂O₃-SnO₂ (ITO) or ZnO-In₂O₃-SnO₂ are the combinational examples of the binary compounds. In addition, ternary compound such as Zn₂In₂O₅ and Zn₃In₂O₆ (zinc indates) and In₄Sn₃O₁₂ (indium stannate) is also practically useful to derive being contained in ZnO-In₂O₃ and In₂O₃-SnO₂ systems as shown the figure. In progress, the multi-compound oxides are derived based

on these ternary compounds such as $Zn_2In_2O_5$ – $In_4Sn_3O_{12}$ to find the reduced indium TCO thin film for the economic application.

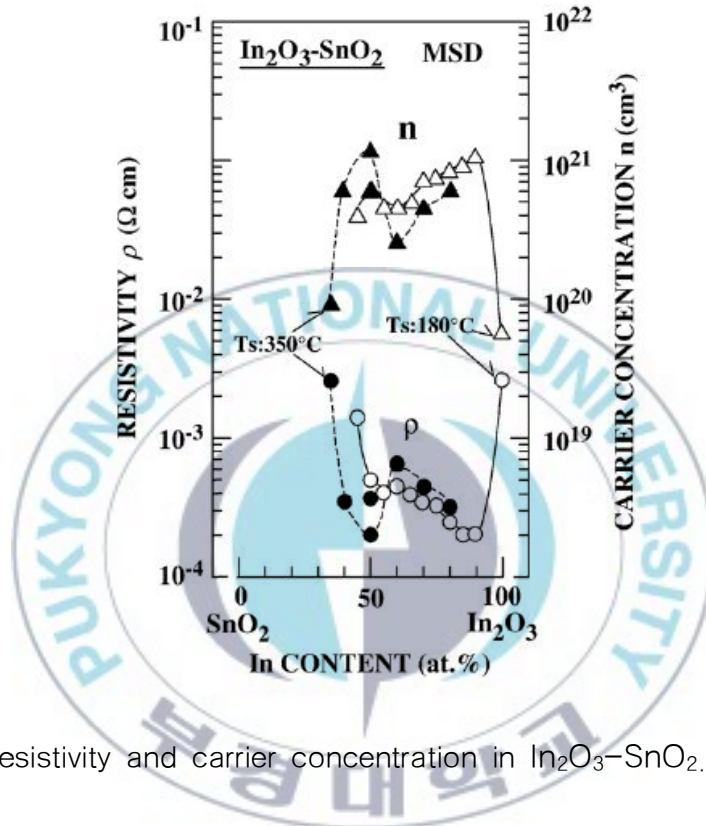


Fig.23 Resistivity and carrier concentration in In_2O_3 – SnO_2 . compound

This above figure shows the electric resistivity and the electric charge carrier concentration as functions of Indium content for the In_2O_3 – SnO_2 . compound material. The electric resistivity of ITO is decreasing ρ with the increased content of indium amount. Two electric resistivity minima corresponding two different maximum carrier concentrations exist. Those are the indium contents around

50 atm. % and 90–95 atm. % depending on the formation temperature.

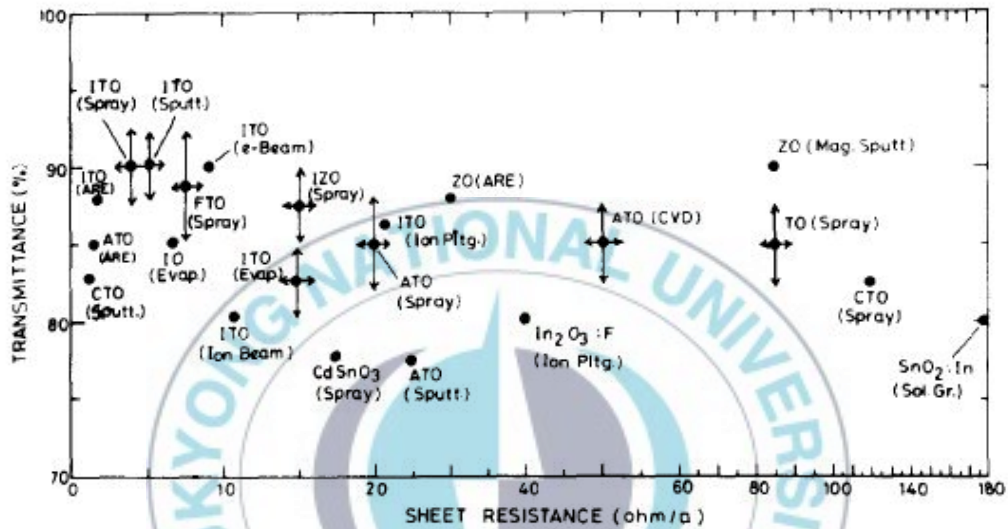


Fig.24. Resistivity and carrier concentration in $\text{In}_2\text{O}_3\text{-SnO}_2$ compound

Fig.24 show that a typically obtained for some of the useful transparent conducting oxides prepared by various material fabrication techniques. The usual abbreviations for the different techniques have been used. The bars show the fluctuations in comparable data reported by various workers.

Under optimum conditions of deposition undoped TO (Tin

Oxide) films are generally polycrystalline (grain size, about 20~30 nm) and retain the tetragonal rutile structure of bulk SnO₂. The existence of a preferred orientation of the crystallites and its dependence on substrate temperature and on oxygen partial pressure (in the case of sputtering) is well established, although reports on the exact nature of the orientation lack consistency. As already mentioned, the presence of the SnO phase and the stoichiometry in reactively sputtered films depend on several deposition parameters. For films prepared by CVD or by spraying, the reports on the presence of the SnO phase are quite conflicting. The n-type conductivity of undoped SnO₂ is primarily due to its nonstoichiometry, but in films deposited from chlorides the incorporation of chlorine ions into the lattice also contributes to the conductivity. SnO₂ films are degenerate semiconductors, typically with a carrier concentration $N = 10^{19} \sim 10^{20} \text{ cm}^{-3}$, a mobility $\mu = 5 \sim 30 \text{ cm}^2 \text{ V}^{-1} \text{ s}^{-1}$ and a resistivity $\rho = 10^{-3} \sim 10^{-2} \text{ } \Omega \cdot \text{cm}$

Annealing of SnO₂ films at 400°C in oxidizing or reducing ambients causes a large change in ρ while N remains weakly affected. Figure 5 shows the typical behaviour of ρ on annealing in vacuum and air. It is concluded that the chemisorption or desorption of oxygen, primarily from the grain boundaries, controls this behaviour and accounts for the lack of thermal stability of the

electrical parameters.

IO (Indium Oxide) films are generally polycrystalline with a cubic bixbyte structure in the bulk material and with little change in the lattice parameter ($a = 10.118 \text{ \AA}$). Muller has reported a typical grain size of about 100 \AA for reactively sputtered films. The lattice (100) or (111) preferred orientation has generally been reported in these films which have been obtained by various techniques. The superiority of IO over TO films as transparent conductors is largely due to the higher mobility in IO. IO films prepared by various techniques have mobilities in the range $10 \sim 75 \text{ cm}^2 \text{ V}^{-1} \text{ s}^{-1}$, with $N = 10^{19} \sim 10^{20} \text{ cm}^{-3}$. Better results are obtained after a reducing heat treatment which improves the conductivity. A subsequent oxidizing heat treatment has been found to result in a decrease in conductivity.

Of special note is a recent report who have deposited pure In_2O_3 films by evaporating a mixture of In_2O_3 10 wt.% In in an oxygen ambient at 340°C . The as deposited films had the sheet resistivity of about $74 \text{ cm}^2 \text{ V}^{-1} \text{ s}^{-1}$ and the transmission is approximately $\sim 90\%$. These are the best values obtained for any undoped transparent conductor and rival those for the ITO system very closely. ITO films exhibit a direct optical band gap which lies between 3.55 and 3.75 eV as reported by several workers and

which has been shown to increase with increasing carrier concentration. The optical transmission in the visible and near IR regions is about 75% ~ 90%. The refractive index in the visible region ranges between 1.9 and 2.08. Muller has reported an effective mass $m^* = 0.3 m_e$ for the conduction electrons.

3.5. Material properties of carbon nanotube [19–26, 46–49]

3.5.1 Atomic structure of carbon nano tube

The atomic structure of nano tubes can be described in terms of the tube chirality or helicity which is defined by the chiral vector \vec{C}_h and chiral angle θ

$$\vec{C}_h = n\vec{a}_1 + m\vec{a}_2 \quad (19)$$

where the integer (n,m) are the number of steps along the zig-zag carbon bonds of the hexagonal lattice and \vec{a}_1 and \vec{a}_2 are unit vectors as shown on the below figure.

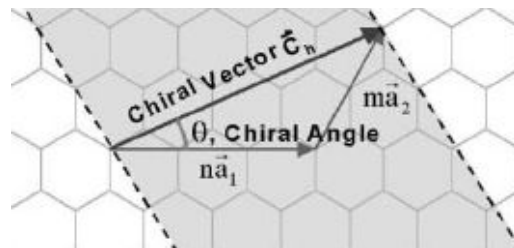


Fig.25 Hexagonal sheet of graphite to form a carbon nanotube

The chiral angle determine the amount of twist in nono tube structure. Two limiting case exist where the chiral angle is at 0° and 30° . The angle of 0° is referred to as zig-zag carbon bond while the angle of 30° is referred to armchair based on the geometry of the carbon bonds as shown on the figure.



Fig.26 Zig-zag carbon bond (a) and Arm-chair carbon bond (b)

Nanotubes exist either single wall or multi wall structures. Multi-walled carbon nanotubes (MWCNTs) are simply consisting of concentrically overlapped single-walled carbon nanotubes (SWCNTs)

3.5.2 Properties of carbon nano tube

Many researchers have reported mechanical properties of carbon nanotubes that exceed those of any previously existing

materials. The reported mechanical strengths is approximately 10 ~100 times higher than the strongest steel at a fraction of the weight. In addition to the exceptional mechanical properties associated with carbon nanotubes, they also possess superior thermal and electric properties [19–26].

Carbon nano tubes are thermally stable up to 2,800 °C in vacuum, thermal conductivity about twice as high as diamond. For the electric property, the electric-current-carrying capacity is 1,000 times higher than copper wires [46].

These exceptional properties of carbon nano tubes have been investigated for devices such as field-emission displays, scanning probe microscopy tips, and micro-electronic devices [47–49].

To commercialize CNTs into the industry application, there are two aspects generally described on literature in terms of CNT dispersion. Because CNT has a graphene structure whose nature is non-polar thus it's natural that carbon nano tube re-agglomerates once it's dispersed into matrix

1. Isolated by Mechanical means
2. Enhancing Dispersion stability

Firstly, to isolate the contents of CNTs, ultra-sonic or super-sonic method, homogenizer and milling process can be use

based on the mechanical treatments. Secondly, in order to enhance dispersion stability of CNTs , the commonly mentioned methods are to use in-situ reaction or chemical wrapping. The chemical wrapping is to warp CNT surface with a chemical which has chemical affinity with the matrix.



4. EXPERIMENTAL PROCEDURES

4.1. Material preparation for the EL film structure

4.1.1. ZnS-based phosphor added Carbon Nanotubes

The commercially available ZnS-based phosphor, more specifically ZnS:(Cu, Al) green-emission phosphor and CNT (multiwall CNT IL-Jin Nano Tech. Co.) was used for the main layer material of composites. CNT having 10~20 micro meter in length 4~2 nm in diameter and surfactant (SDS; $\text{CH}_3(\text{CH}_2)_{11}\text{OSO}_3\text{Na}$) were ball milled with isopropyl alcohol(IPA) for 24 hours in order to implant CNT dispersedly into ZnS-based phosphor surface where the ratio of CNT to surfactant was 1:5. The weight ratio of CNT to phosphor was varies from 0.25 to 1 wt% ZnS: (Cu, Al).

4.1.2. ZnS-based phosphor inserted Transparent Conductive Oxide (TCO)

Transparent conductive oxide (TCO) materials such as In_2O_3 (99.9%) and SnO_2 (99.99%) are used to investigate the impurity effect with the phosphor layer. In_2O_3 and SnO_2 powder and the surfactant (SDS; $\text{CH}_3(\text{CH}_2)_{11}\text{OSO}_3\text{Na}$) are ball milled with isopropyl alcohol (IPA) for 24 hours to homogeneously disperse into ZnS-based phosphor, respectively. The weight ratio of TCO materials to ZnS phosphor is varies from 0.25 wt. % to 1.5 wt. %. To form screen printable

dielectric material layer, approximate 50~60 wt. % of BaTiO₃ having the particle size of 0.4~1.2 μ m is mixed with the binder material of Thermoplastic Vinyl also available in commercial.

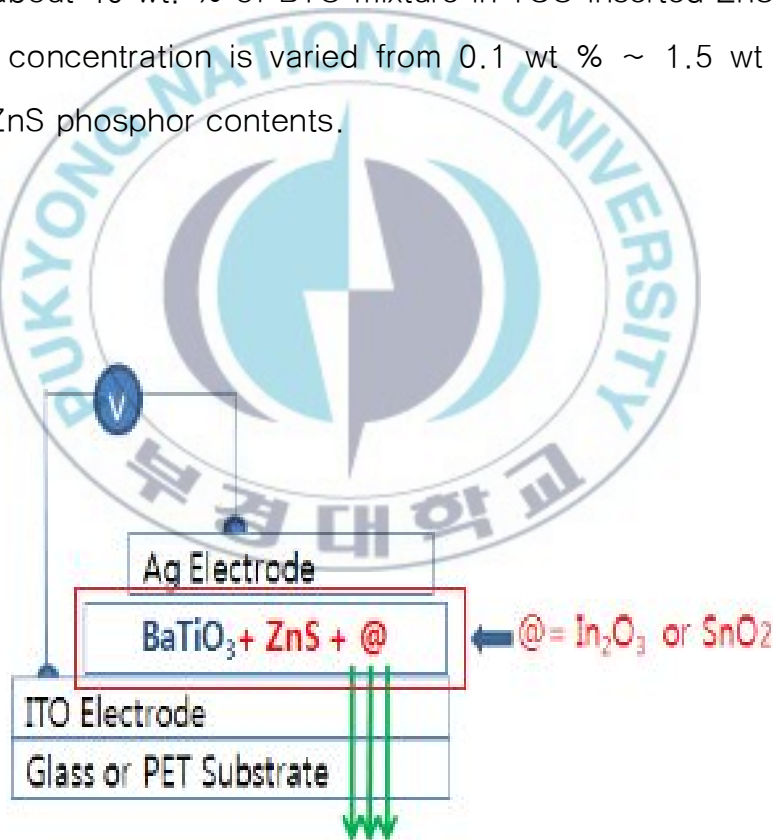
4.2. Fabrication of the EL film structure

Commercially available screen net made of polyester having mono filament type is used for the screen printing apparatus. The screen size of 180 mesh and the snap-off distance 2 mm are maintained while in the whole film fabrication. The optimum condition for the squeeze angle and the printing speed are empirically evaluated by the repeated procedure in advance for the uniform film thickness control. The phosphor layer and the dielectric layer are screen printed with the same area but the areal size of Ag Electrode is 70% of the active layer to prevent electric shortage. The thickness of screen printed layer is controlled by the film thickness measuring gauge and each printed layer is stabilized with the annealing machine with temperature of 150°C and 20 min. annealing time after a film screen printout.

In this experiment, two different layer structures of EL device, namely 1 layered structure and 2 layered structure are introduced to the enhanced EL intensity in connection with the TCO insertion in ZnS-based EL device.

As shown on Fig. 27, the 1 layered structure is related to 2 stage printing process. First, the hybrid layer is screen printed on In ITO substrate, and then the Ag-electrode layer is formed also using the screen printing. The printed hybrid layer on ITO substrate consists dielectric material of BaTiO_3 mixed into the TCO inserted ZnS-based phosphor material. The material composition of the hybrid layer comprises about 40 wt. % of BTO mixture in TCO inserted ZnS-based resin. TCO concentration is varied from 0.1 wt % ~ 1.5 wt % with respect to ZnS phosphor contents.

(a)



(b)

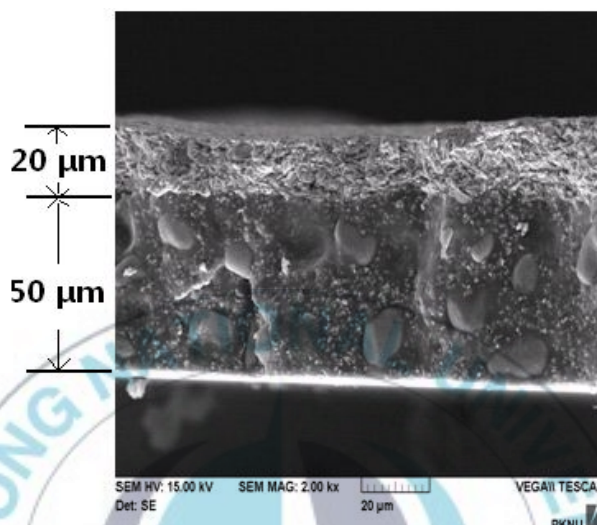
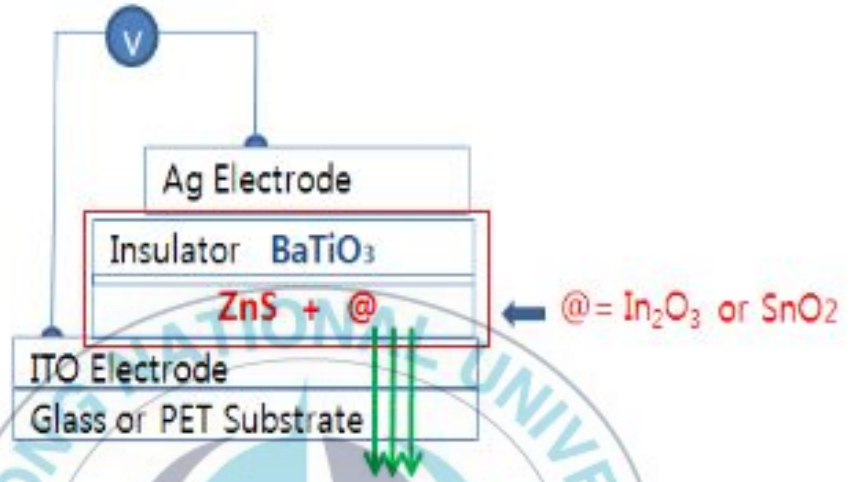


Fig. 27. (a) 1-layered EL structure and (b) its cross sectional view of SEM

As shown on Fig. 28, the 2 layered structure is related to 3 stage process to complete EL device as follow ; (1) the TCO inserted ZnS-based phosphor layer is screen-printed on ITO substrate, (2) a separate dielectric layer formed on the TCO inserted ZnS layer also using screen printing and then (3) finally Ag-electrode layer is screen-printed. The TCO insertion is varied from 0.1 wt % ~ 1.5 wt % with respect to ZnS phosphor contents ,and approximate 50~60 wt. % of BaTiO₃ mixed with the binder available in commercial are used for screen printing the 2 layered structure.

(a)



(b)

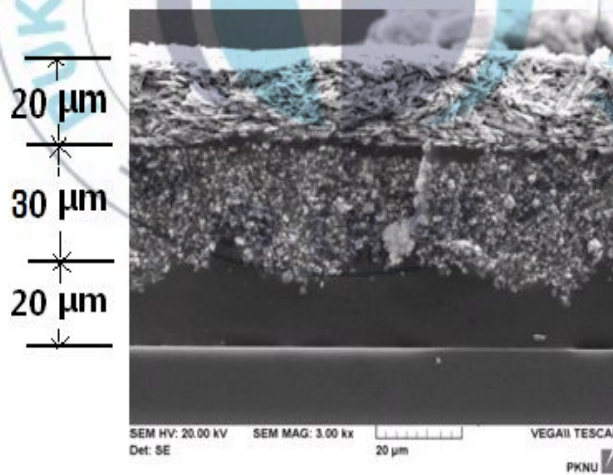


Fig. 28. (a) 2-layered EL structure and (b) its cross sectional view of SEM

5. RESULTS AND DISCUSSION

5.1. CNT doped ZnS based EL Devices.

The XRD spectrum shows as shown in Fig. 29, the most probable XRD patterns of the dispersed CNT in the ZnS phosphor carried out to confirm the concentration dependency of CNT dispersed in the host phosphor ZnS using a Ni-filtered Cu K α radiation in a diffractometer (Rigaku. D/Max 2500). Obviously CNT does not effect the crystalline structure of the phosphor composites that remains the cubic lattice structure and conforms well with JCPDS #77-2100.

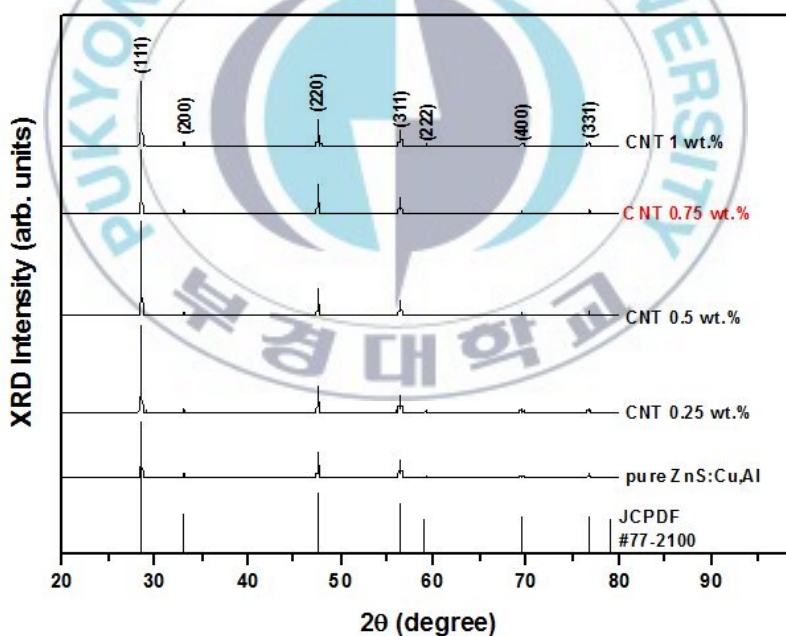


Fig. 29. XRD patterns depending on the CNT concentration in ZnS:(Cu, Al)

As seen on Fig. 30, FE-SEM (JEOL JSM-6700F) images are investigated in order to verify presence of CNT element and morphology of the dispersedly implanted CNT in ZnS-based phosphor. As expected, the CNT dispersed on to surface of ZnS based phosphor has reveals an implanted type on ZnS based Phosphor surface rather than a necklace type or a coated type on ZnS-based phosphor usually observable in the metal-CNT or semimetal-CNT composites.

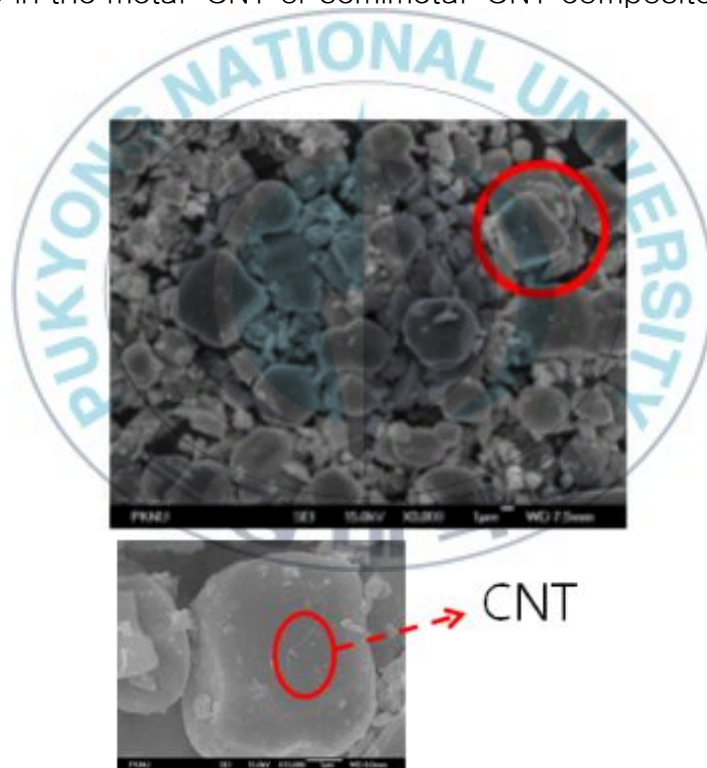


Fig. 30. SEM images of CNT impurity doped ZnS:(Cu, Al)

Fig. 31 and Fig 32 show the electrooluminescence spectra of CNT free- and CNT doped-ZnS:(Cu, Al) EL device as function of operating voltage, respectively. An optimal concentration of CNT in the phosphor is 0.75 atm.% and CNT concentration is fixed at 0.75 atm.% in all EL devices.

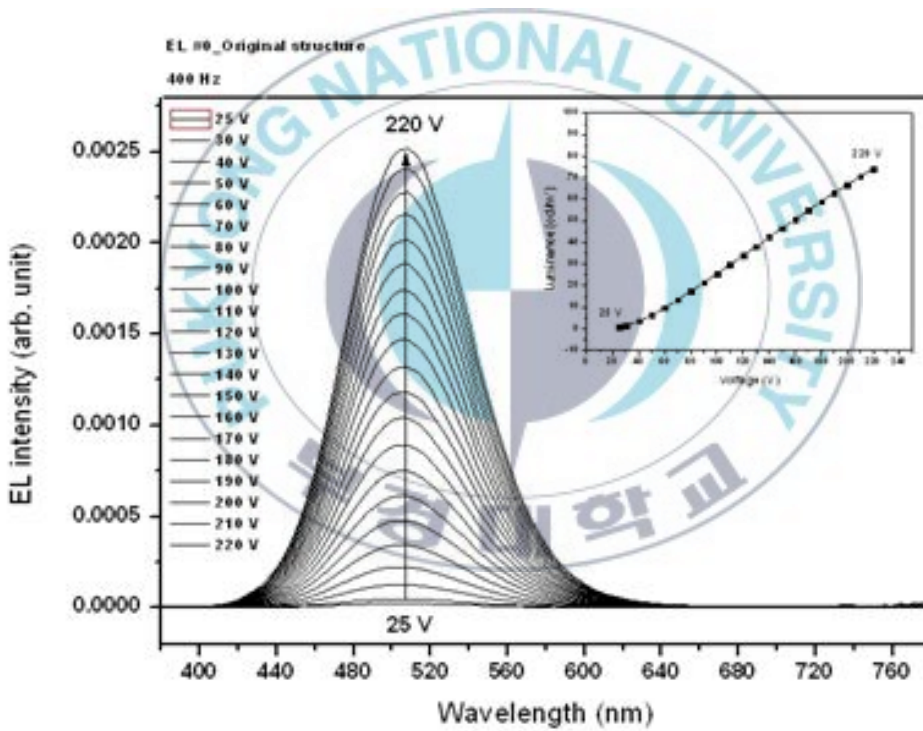


Fig. 31. EL spectra of CNT free-ZnS:(Cu, Al) EL Device

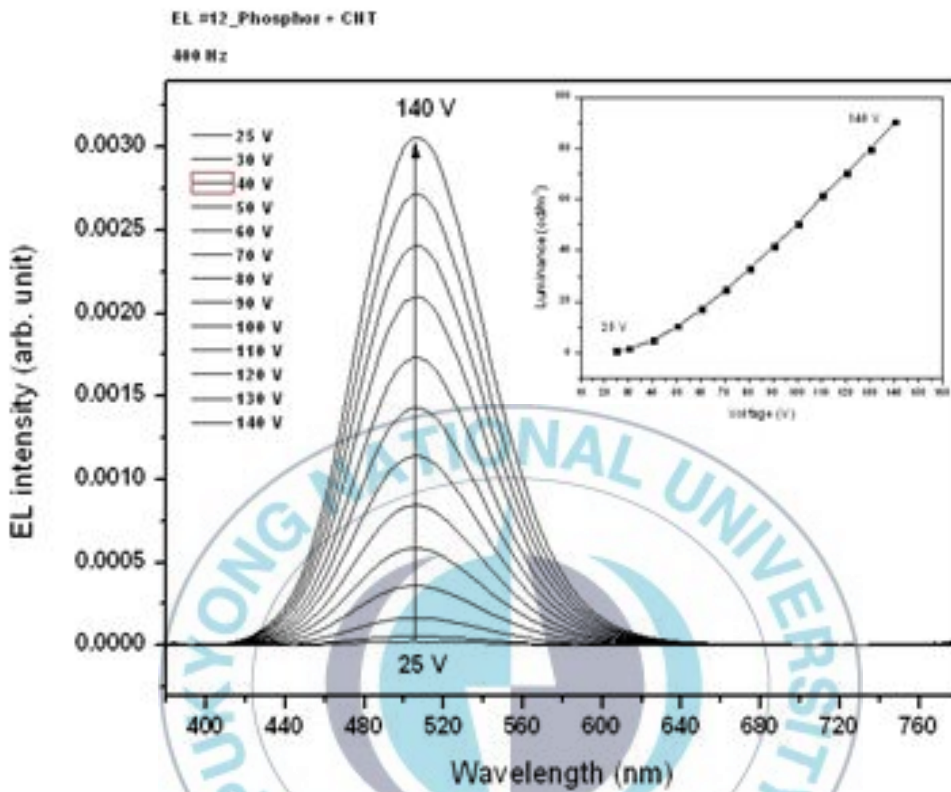


Fig.32.EL spectra of CNT doped-ZnS:(Cu, Al) EL Device

According to our empirical data related to the EL thin layers for electric and optical measurements, an optimum thickness of the CNT doped-ZnS: (Cu,Al) phosphor layer is approximately 50 micro-meter and the buffer insulator layer of BaTiO₃ is about 20 micro-meter in our EL device.

EL spectra show green emission peaking at 515 nm due to the donor-acceptor (DA) pair transition between the donor of Cu and the

acceptor of Al in the ZnS host phosphor. Operating voltage of EL device fabricated CNT doped-ZnS:(Cu, Al) is lower than that of CNT free-ZnS:(Cu, Al) EL device as seen in fig. 31 and 32. It can be explained that clearly CNT element contributes the EL mechanism providing a pathway or channel for creation of hot electrons and a pathway of electron-hole recombination through the luminescence process. Fig. 33 shows photograph of our EL device using a CNT doped-ZnS:(Cu, Al) phosphor, we can see bright green luminescence.



Fig.33. Photograph of emitting EL device using a CNT doped-ZnS:(Cu, Al) phosphor

5.2. TCO doped ZnS based EL Devices

Fig. 34 shows that experimental results of the critical voltages depending on the layer thickness of BaTiO₃ under the device

structure having a separate dielectric layer as shown Fig. 28. According the results, the deviation of the threshold voltages to emit EL spectrum is relatively small with respect to the deviation of the shutdown voltages to breakdown the EL device as shown Fig 34.

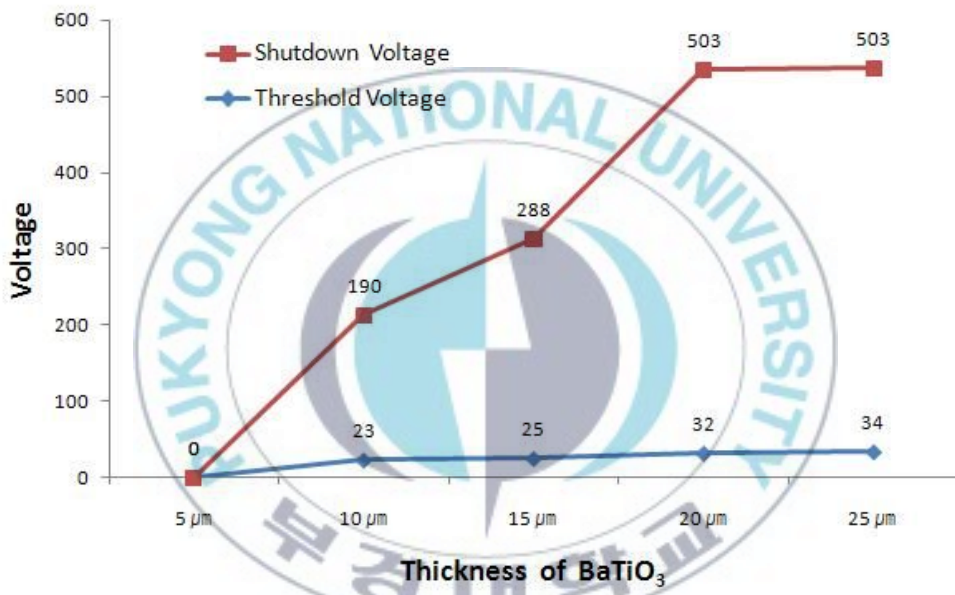


Fig. 34. Critical voltages depending on BaTiO₃ layer in TCO doped-ZnS:(Cu, Al) EL device

These experimental results mean that thicker layer of BaTiO₃ relates higher breakdown voltage but thinner layer of BaTiO₃ is related to lower threshold voltage. From these experiment results, the optimum thickness of dielectric layer BaTiO₃ 20 μm is determined.

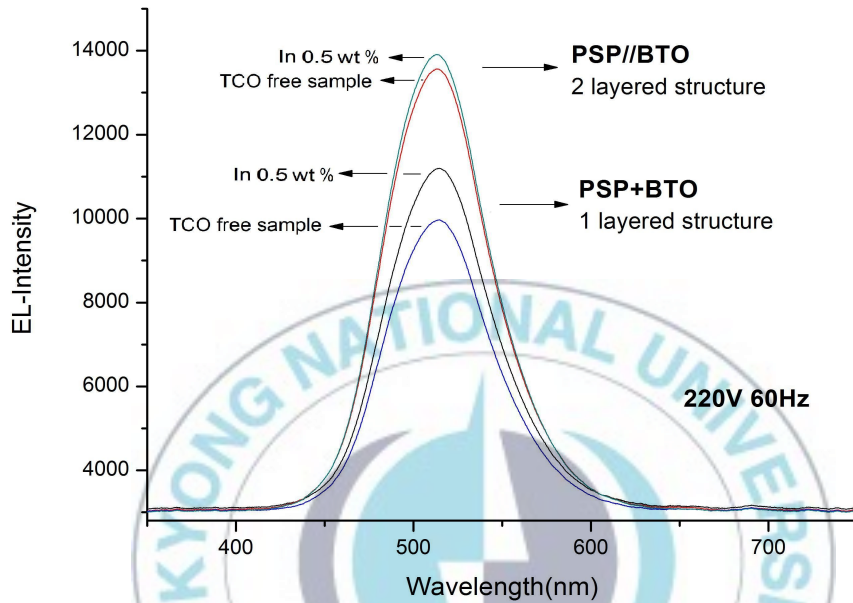


Fig. 35. EL intensity depending on the layered structure in ZnS:(Cu, Al) EL device

Fig. 35 is measured EL spectrums depending on the layered structure. Basically the layered structure under this experiment is classified whether a separate BaTiO₃ layer is exist or not. 2 layered structure as shown on Fig. 28 has a separate BaTiO₃ layer but 1 layered structure as seen on Fig. 27 has no separate dielectric layer BaTiO₃. Luminescence intensity of the 3 layered structure is 1.4 times greater than the 2 layer structure under the external force 220V 60 Hz.

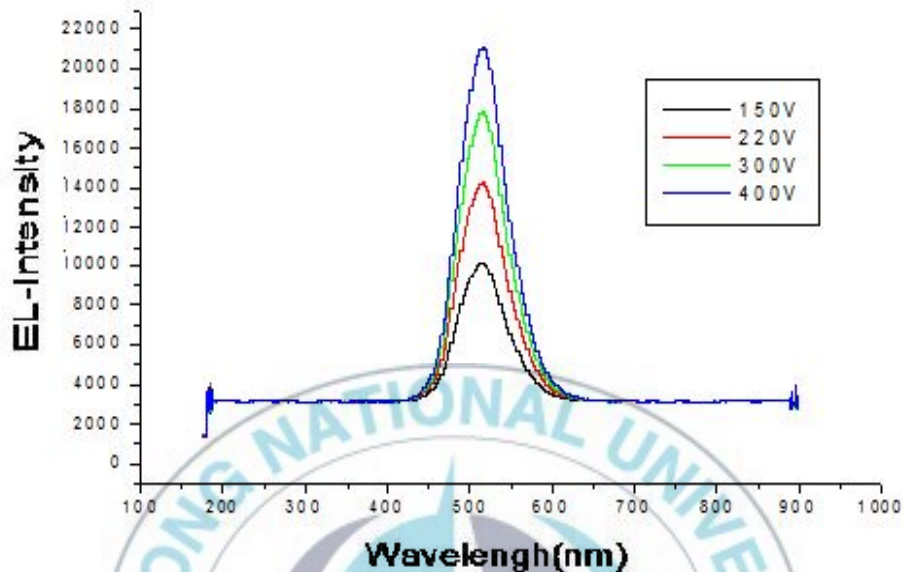


Fig. 36. EL intensity depending on the applied voltages in ZnS:(Cu, Al) EL device

Fig.36 show that EL spectrums depending on the applied voltage from 150 V 400 V. EL spectrums from all ZnS-based phosphor are 514nm green emission in common as expected. The luminescence center is originated from Al Donor to Cl Acceptor impurities (D-A pair emission) in ZnS based phosphor. The maximum EL intensity measured from the external force 400 V is 2.2 times higher than that of 150 V. The EL intensity is linearly increasing with the applied external voltage from 30 V to 500V along the 3 layered sample structure.

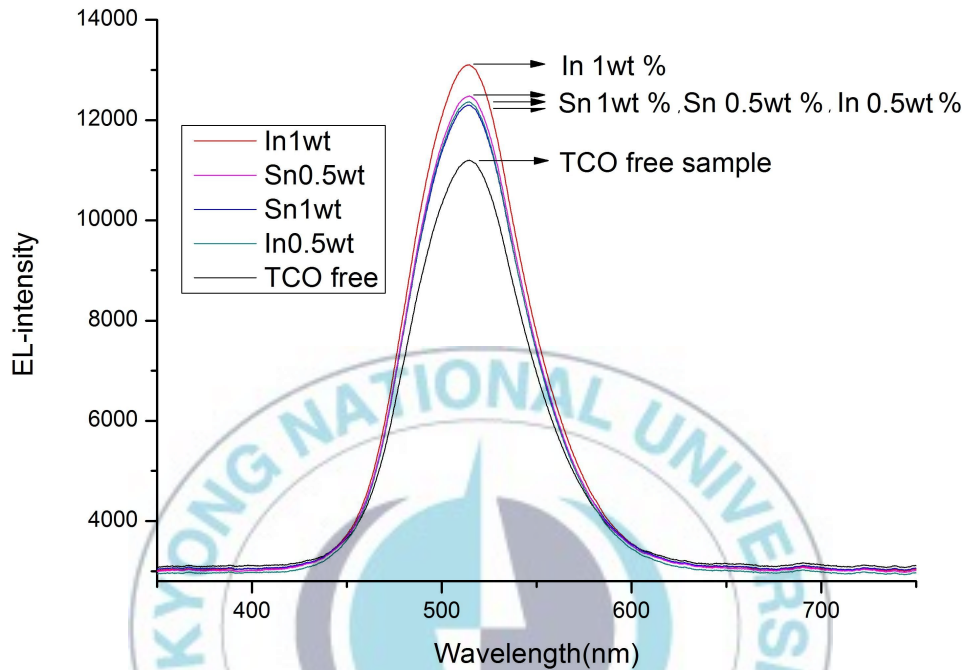


Fig. 37. EL intensity of ZnS:(Cu, Al) layer depending on the inserted In_2O_3 and SnO_2

Fig.37 show the enhanced luminescence caused by the transparent conductive oxide In_2O_3 and SnO_2 , the Indium oxide is more effective than tin oxide material to enhance the EL intensity. The best optimum concentration is indium oxide 1 wt.% but overly inserted indium oxides approximately 2~3 wt.% causes electric breakdown in the ZnS based layer. The enhance EL intensity is approximately 1.2 times greater than the TCO free samples (Normal) as shown on Fig. 37

under the external 220 V, 60Hz. In_2O_3 and SnO_2 is known as TCO (transparent conductive oxides) materials because it has high electrical conductivity having over 80% transparent property in 400nm ~800nm visible light. From these experiment results whether 2 or 3 basic layered structure, the inserted TCO into ZnS based EL layer might be a positive additive to enhance the entire EL intensity.

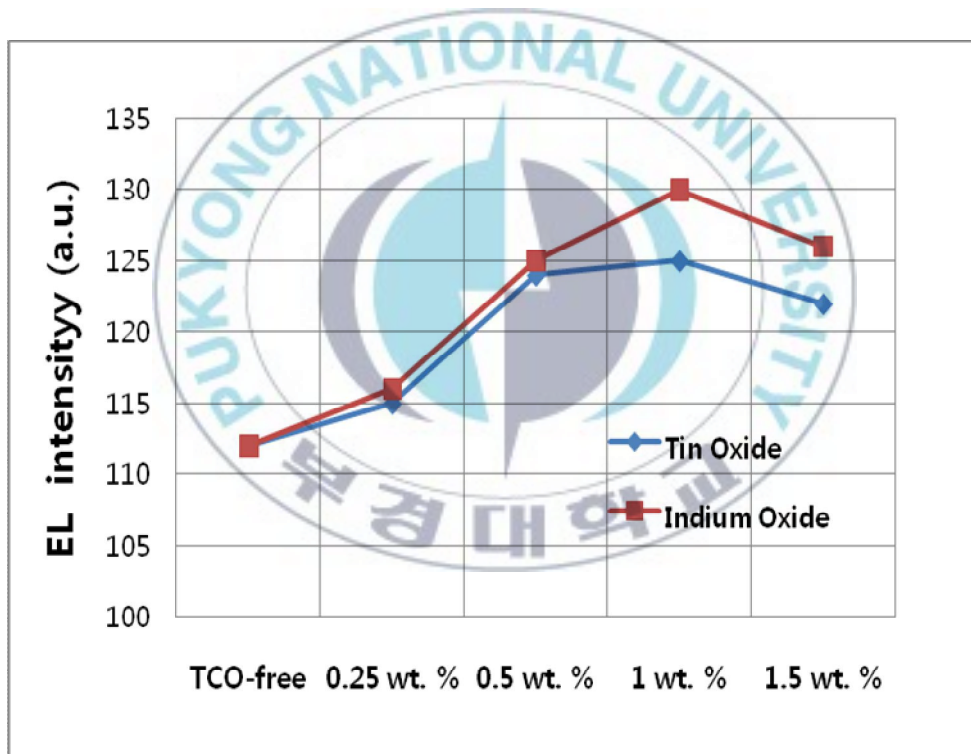


Fig. 38. Compared EL intensities under 1-layer structure depending on the inserted In_2O_3 and SnO_2

Fig.38 is a summarized result of EL enhancement depending on the inserted In_2O_3 and SnO_2 under the 1-layered structure. The EL intensity is increased by the increase of TCOs concentration up to 1 wt.%. The TCO of In_2O_3 shows more likely to enhance the EL emission than the SnO_2 but the detail analysis remains in our task to challenge. The overly doped TCO of more than 1.5 wt.% shows unstable EL emission due to the electric short.

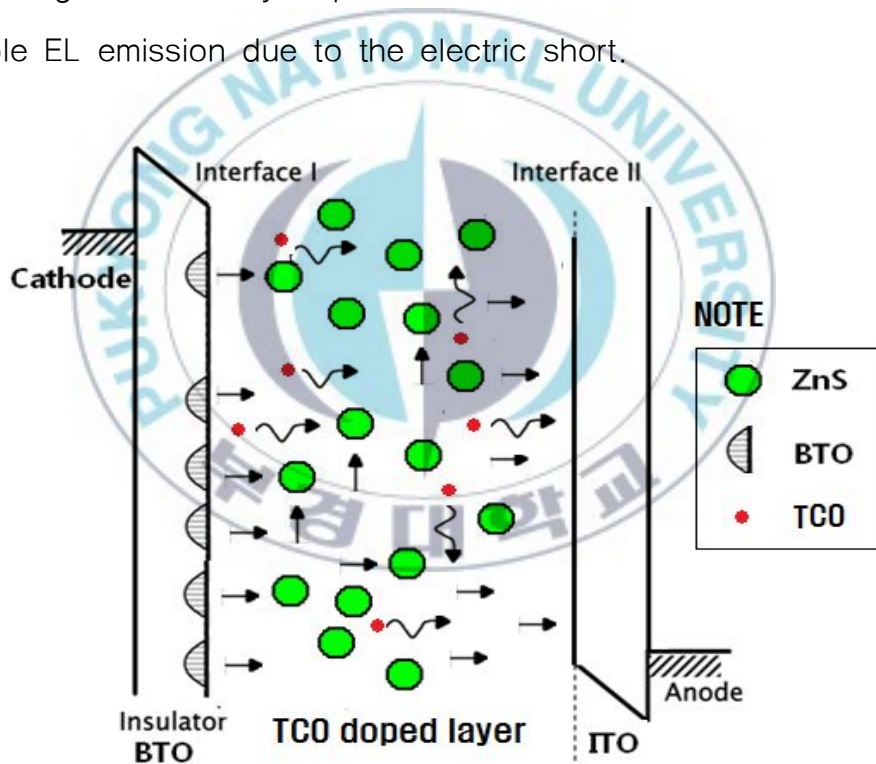


Fig. 39. Schematic showing electron flow under the 2 basic layered structure

As shown on Fig.39, it is useful to consider a schematic view of electron flow under the basic layered structure to confirm the luminescence mechanism in connection with the film structure and the material constitution. Interfacial effects of the phosphor (ZnS)–dielectric (BTO) interface are crucial in that the interfacial surface provides trapping sites of electron carriers, and the trapped electron carriers in the interfacial surface increase the number of EHP(Electron Hole Pair) in the donor(Al)–acceptor(Cl) level intrinsically doped in ZnS phosphor thereby activate the avalanche breakdown with the external force to effect the electro luminescence output. All EL spectrums from ZnS–based phosphor is 514 nm green emission. The green luminescence center is originated from D–A pair emission in ZnS based phosphor.

To increase the trapped injection electrons in the interfacial surface and to provide effective pathways for the injection electron flow, TCO is inserted into the ZnS–based phosphor resin. As shown on the drawing, TCO provides gateways activated by the electron–TCO scattering in the phosphor resin so that the injection electrons can easily access ZnS–based phosphor to create EHPs in the ZnS–based phosphor resin [50]. The emitted photons from ZnS–based phosphor are not disturbed or absorbed by the inserted activator TCO in the emission layer due to the high transparent property (over 80% in

400nm ~800nm visible light)

But the particle concentration of the conductive element In_2O_3 or SnO_2 in the ZnS-based resin is necessary to adjust to find an optimum insertion so that no complete conducting path is occurred between Ag and ITO electrode to prevent the electric short. Based on this experiment results, over 3 wt%~4 wt% TCO create probable electric shorts and unstable EL emissions.

Similarly, as shown on Fig. 40, it is also useful to consider a schematic view of electron flow under the 2 basic layered structure to confirm the luminescence mechanism in connection with the film structure and the material constitution.

The luminescence center of ZnS-based phosphor powder is surrounded by dielectric BaTiO_3 resin. When the external voltage is applied, Electron-Hole Pairs (EHPs) in ZnS-based phosphor are created by the injection electrons from the carrier electrons trapped in the dielectric (BTO) resin. In this hybrid layer under the 1 layered structure, an optimum concentration TCO of In_2O_3 or SnO_2 is about 1 wt.% according to our experiment.

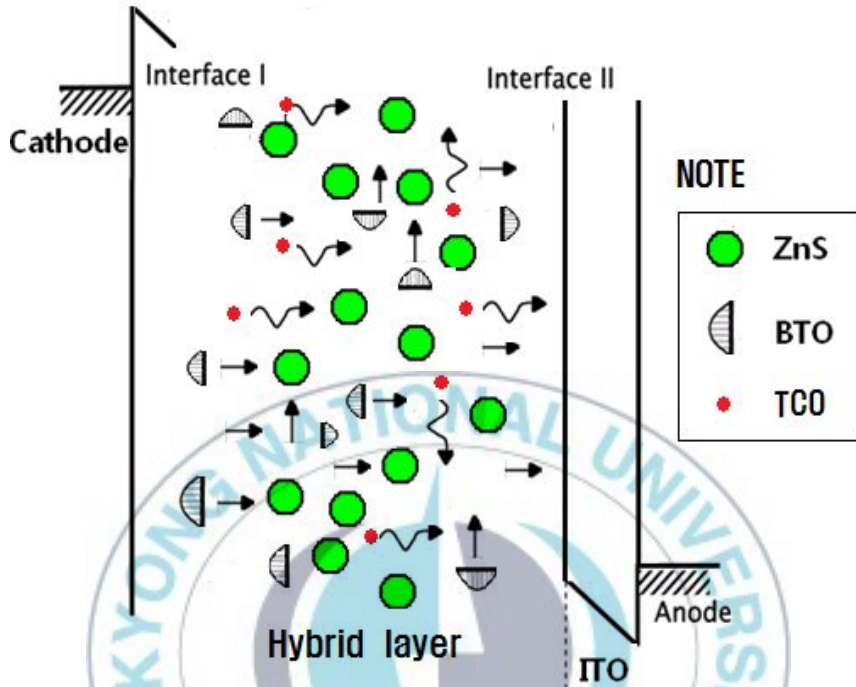


Fig.40. Schematic showing electron flow under the 1 basic layered structure

The optimum TCO provide gateways from the trapped electrons in BTO to ZnS-based phosphor to accelerate the injection electrons caused by the applied electric field. As discussed with Fig 39, overly doped In_2O_3 or SnO_2 embedded in the dielectric BaTiO_3 resin can produce electrically conducting paths penetrating BaTiO_3 dielectric medium between ITO substrate and Ag electrode. This causes more probable electric shorts and unstable EL emissions under the applied

voltage.

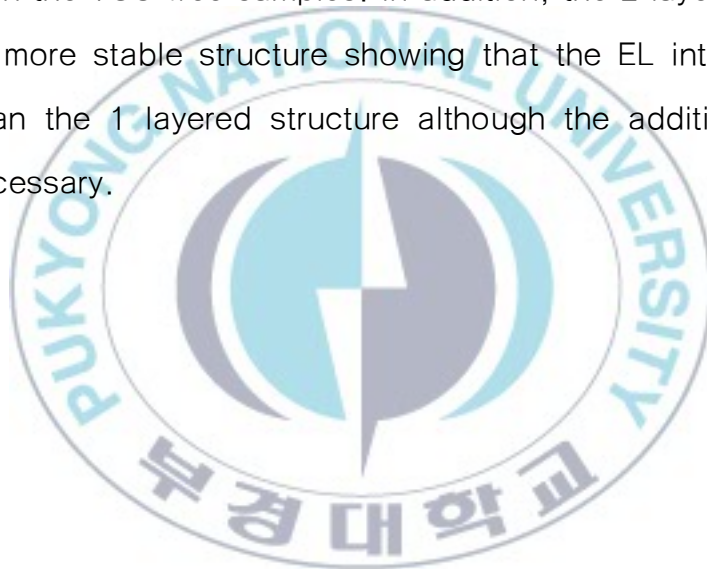
The increased EHPs in the ZnS-based phosphor enhance the EL intensity as expected. This simplified 1 layered structure of EL can be understood with the formation of grain boundaries surrounding the ZnS based phosphor point sources rather than the interfacial surface of phosphor-dielectric model as described in the 2 layered structure. The trapped carriers in the interfacial surface of the dielectric-phosphor can be interpreted as trapped electrons in the grain boundary of phosphor surrounded by dielectric medium. Accordingly we can understand that the enhanced luminescence effects caused by injection electrons trapped in the grain boundary under the architecture of 1 layered are same phenomena in principle as described in the interfacial surface of phosphor-dielectric model as shown on the 2 layered structure of EL device.

6. CONCLUSIONS

The studies on Electro-luminescence effect of impurity ZnS thin film structure fabricated by Screen Printing Method can be summarized as followings.

(1) We confirmed that an optimum value of CNT concentration in the ZnS:(Cu, Al) film panel is about 0.75 atm % resulting that the electric conductivity is 1.6 times higher than that of pure CNT sample and showing that the luminescence intensity is increasing until the optimum concentration. Clearly, CNT is presenting in the luminescence process providing a pathway for the creation of hot electron and a channel for the electron-hole recombination but overly inserted CNT may hinder to produce the hot electron for making an avalanching process. In case of the overly doped CNT 0.1 atm % in the ZnS-based phosphor, the luminescence intensity is decreasing although the electric conductivity is exponentially increasing. Based on these results, we realized that hot electron occurred by the external electric field or exciton arose by the external photon source are reduced dramatically over the critical value of CNT concentration because CNT element provide various isolated residue in the composites of ZnS based phosphor rather than pathway or channel for the D-A (Donnor to Acceptor) pair transition or the radiative recombination of electron-hole.

(2) Clearly, we can conclude that TCO like In_2O_3 , or SnO_2 is presenting in the luminescence process providing gateways activated by the injection electron-TCO scattering in the phosphor resin so that the injection electrons can easily access ZnS-based phosphor to create EHPs in the ZnS-based phosphor resin. The enhance EL intensity under the optimum TCO insertion is approximately 1.2 times greater than the TCO free samples. In addition, the 2 layered structure has also more stable structure showing that the EL intensity is 1.4 greater than the 1 layered structure although the addition dielectric layer is necessary.



REFERENCES

- [1] G.Destriau, J. Chem. Phys., 33, 587 (1936).
- [2] P.Kahng, Appl. Phys. Lett., 13, 210 (1968).
- [3] S.Mito, C.Suzuki, Y.Kanatani, and M.Ise, Digest of 1974 SID International Smposium, 86 (1974).
- [4] A.N.Krasnov, Displays, 24, 73–79 (2003).
- [5] G.Sharma, S.D.Han, J.D.Kim, S.P.Khatkar, and Y.W.Rhee, Mater. Sci. Eng. B 131, 271–276 (2006).
- [6] Y.T.Nien, I.G.Chen, C.S.Hwang, and S.Y.Chu, J. Phys. and Chem. of Solids, 69, 366–371 (2008).
- [7] T.Toyama, T.Hama, D.Adachi, Y.Nakachizu, and H.Okamoto, Nanotechnol., 20, 055201 (2009).
- [8] H.D.Golderg, R.B.Brown, D.P.Liu, and M.E.Meyerhoff, Sensors and Actuators B, 21, 171–183 (1994).
- [9] G.E.Jabbour, R.Radspinner, and N.Peyghambarian, IEEE Quantum electronics, 7, 769 (2001).
- [10] G.Blanchet, J.Rogers, J. Image Sci. Tech., 47, 296 (2003).
- [11] S.E. Shaheen, R.Radspinner, N.Peyghambarian, and G.E.Jabbour, Appl. Phys. Lett., 79, 2996 (2001).
- [12] D.H.Lee, J.Choi, H.Chae, C.H.Chung, and S.M.Cho, Korean J. Chem. Eng., 25 176–180 (2008).
- [13] V.Kumar, M.K.Sharma, J.Gaur, and T.P.Sharma, Chalcogenide

Letters, 5, 289 (2008).

[14] T.M.Lee, Y.J.Choi, S.Y.Nam, C.W.You, D.Y.Na, H.C.Choi, D.Y.Shin, K.Y.Kim, and K.I.Jung, *Thin Solid Films*, 516, 7875 (2008).

[15] J.Y.Kim, S.H.Park, T.Jeong, M.J.Bae, S.Song, J.Lee, I.T.Han, D.Jung, and S.Yu, *IEEE Transactions on Electron Devices*, 57, 1470 (2010).

[16] C.C.Kao, Y.C.Liu, *Mater. Chem. Phys.*, 115, 463–466 (2009).

[17] S.J.Lee, J.E.Jang, Y.W.Jin, G.S.Park, S.H.Park, N.H.Kwon, Y.J.Park, J.E.Jung, N.S.Lee, J.B.Yoo, J.H.You, and J.M.Kim, *J. Electrochem. Soc.*, 148, H139–H142 (2001).

[18] K.Manzoor, V.Aditya, S.R.Vadera, N.Kumar, T.R.N.Kutty, *Appl. Surf. Sci.*, 252, 3968–3971 (2006).

[19] S. Iijima, *Nature*, 354, 56 (1991).

[20] H. Dai, E. W. Wong, and C. M. Lieber, *Science* 272, 523 (1996).

[21] S. Berber, Y.-K. Kwon, and D. Tománek, *Phys. Rev. Lett.* 84, 4613 (2000).

[22] M. M. J. Treacy, T. W. Ebbesen, and J. M. Gibson, *Nature* 381, 678 (1996).

[23] W. A. de Heer, A. Chatelain, and D. Ugarte, *Science* 270, 1179 (1995).

[24] M.J.Bae, S.H.Park, T.W.Jeong, J.H.Lee, I.T.Han, Y.W.Jin, J.M.Kim, J.B.Yoo, and S.G.Yu, *Appl. Phys. Lett.*, 95, 071901

(2009).

[25] D.S.Hecht, L.Hu, G.Gruner, Current Applied Physics,

[26] J.H.Park, B.W.Park, K.W.Park, J.S.Kim, G.C.Kim, J.H.Yoo, I.Yu, Solid State Communications, 148, 573–576 (2008).

[27] G.J.Exarhos, X.D.Zhou, Thin Solid Films 515, 7025–7052 (2007).

[28] R.G.Gordon, MRS Bulletin, August, 52–57 (2000).

[29] K.G.Cho, D.Kumar, S.L.Jones, D.G.Lee, P.H.Holloway, and R.K.Singh, J. Electrochem. Soc., 145, 3456 (1998).

[30] D.S.Zhang, K.Y.Ko, H.K.Park, D.H.Yoon, and Y.R.Do, J. Electrochem. Soc., 155, J111 (2008).

[31] K.I.Seo, J.H.Park, J.S.Kim, Y.H.Na, J.C.Choi, and J.S.Bae, Solid State Commun., 149, 1578 (2009).

[32] M.Marinsek, K.Zupan, and J.Maeek, J. Power Sources., 106, 178 (2002).

[33] T.Minami, Y.Kuroi, and S.Takata, J. Vac. Sci. Technol. A, 14, 1736 (1996).

[34] Y.A.Ono, "Electroluminescent Displays", World Scientific, Singapore (1995).

[35] A.G.Fischer, J. Electrochem. Soc., 109, 1043 (1962).

- [36] P.D.Rack, P.H.Holloway, Materials Science and Engineering, R21, 171–219 (1998).
- [37] D.R.Askeland, The Science and Engineering of Materials, PWS Publishing, Boston, MA (1994).
- [38] G.Blasse, B.C.Grabmaier, "Luminescent Materials", Springer–Verlag, Berlin–Heidelberg (1994).
- [39] S.Shionoya, W.M.Yen, "Phosphor Handbook", Chemical Rubber, Boca Raton, FL (1998).
- [40] R.Schmidt, A.Basu, A.W.Brinkman, Z.Klusek, W.Kozlowski, S. Datta, A.Stiegelschmitt, A.Roosen, Applied Surface Science 252, 8760 (2006).
- [41] F.O.Adurodija, H.Izumi, T.Ishihara, H.Yoshioka, H.Matsui, Appl. Phys. Lett., 74, 3059 (1999).
- [42] T.Minami, Semicond. Sci. Technol., 20, S35 (2005).
- [43] M.Hiramatsu, K.Imaeda, N.Horio, M.Nawata, J. Vac. Sci. Technol., A, Vac. Surf. Films 16, 669 (1998).
- [44] P.K.Song, M.Watanabe, M.Kon, A.Mitsui, Y.Shigesato, Thin Solid Films 411, 82 (2002).
- [45] T.Minami, J. Vac. Sci. Technol., A, Vac. Surf. Films, 17, 1765 (1996).
- [46] E.T.Thostensona, Z.Renb, T.W.Chou, Composites Science and Technology 61, 1899 (2001).

[47] M.S.Dresselhaus, G.Dresselhaus, P.C.Eklund. Science of fullerenes and carbon nanotubes. San Diego: Academic Press, (1996).

[48] B.I.Yakobson, C.J.Brabec, Physical Review Letters 76(14), 2511 (1996).

[49] B.I.Yakobson, G.Samsonidze, Carbon 38,1675 (2000).

[50] W.E. Howard, O. Sahni and P.M. Alt, J. Appl. Phys., 53, 639 (1982)



국문요약

On Electro-luminescence effect of impurity ZnS thin film
structure fabricated by Screen Printing Method

(스크린 프린팅에 의해 제작된 황화아연(ZnS)계 박막의
불순물첨가에 의한 전계발광 효과에 관한 연구)

스크린 프린팅 박막 제작 방법으로 황화아연계 ZnS(Cu, Al) 박막에 카본나노튜브(CNT) 또는 전도성투명산화물(TCO)인 인듐산화물(In_2O_3) 이나 주석산화물 (SnO_2) 불순물을 첨가하여 절연층 복합 구조 또는 절연층 분리구조를 가진 황화아연 ZnS(Cu, Al)계 전계발광소자를 각각 제작하고 불순물 첨가에 의한 전계발광 효과를 연구하였다. 전기 광학적인 특성조사를 위해 엑스레이회절실험(X-ray), 전자주사현미경(Scanning Electron Microscope), 분광실험(Photo-luminescence) 및 전계발광측정(Luminescence vs. Voltage)등의 실험을 통해 전계발광 박막필름의 구조와 구성 물질의 변화에 따른 특성 조사를 실시하였다.

전계발광 소자박막에서 가장 좋은 발광효율을 보이는 카본나노튜브(CNT) 농도는 약 0.75 atm%로서 카본나노튜브(CNT)가 없는 순수시료보다 약 1.6배의 높은 전기전도도를 가지고 발광효율이 향상됨을 확인할 수 있었다. 한편 전도성투명산화물(TCO)가 첨가된 황화아연계 ZnS(Cu, Al) 전계발광 박막소자의 경우 인듐산화물(In_2O_3) 또는 주석산화물(SnO_2) 불순물이 약 1 wt.%에서 약 1.2배로 향상된 전계발광효율

을 관측하였다. 또한 전계박막 소자의 발광층이 복합물 구조로 형성된 1 레이어 박막 구조보다 절연층이 분리된 2 레이어 박막 구조에서 약 1.4배 상대적으로 높은 전계발광 세기를 관측할 수 있었다. 불순물 첨가에 의해 전계발광의 효율이 향상된 결과는 바륨티타늄산화물(BaTiO_3) 절연체 경계에 존재하는 전자들이 외부 인가전원에 의해 가속이 되어 터널링 현상을 통해 발광센터에 이르는 과정에서 발광층의 유기 바인더에 첨가 혼합된 카본나노튜브(CNT) 또는 전도성 투명 산화물(TCO)들은 외부 주입 전자들에게 발광센터에 이르는 통로를 제공함으로써 보다 많은 전자들이 황화아연 ZnS(Cu,Al) 발광센터에서 전자-전공 쌍 (Electron-Hole Pair)을 형성케 함으로서 발광 효율을 증대시킴을 알 수 있었다.

핵심되는 말: 전계발광, 스크린 프린팅, 발광소자